Quantifying the Direct Radiative Effect of Stratospheric Aerosols Using Radiative Kernels

Qiurun Yu[1] and Yi Huang[1]

[1]McGill University

August 15, 2024

Abstract

To facilitate the quantification of the stratospheric aerosol radiative effect, this study generates a set of aerosol direct radiative effect (ADRE) kernels based on MERRA-2 reanalysis data. These radiative kernels measure the sensitivities of ADRE to perturbations in scattering and absorbing aerosol optical depth (AOD), respectively. Both broadband and band-by-band radiative kernels are developed to account for the wavelength dependency of ADRE. The broadband kernels are then emulated by a multivariate regression model, which predicts the kernel values from a handful of predictors, including the top-of-atmosphere (TOA) insolation, TOA reflectance, and stratospheric AOD. These kernels offer an efficient and versatile way to assess the ADRE of stratospheric aerosols. The ADREs of the 2022 Hunga volcano eruption and the 2020 Australia wildfire are estimated from the kernels and validated against radiative transfer model-calculated results. The Hunga eruption induced a global mean cooling forcing of -0.46 W/m² throughout 2022, while the Australia wildfire caused a warming forcing of +0.28 W/m² from January to August. The kernel estimation can capture over 90% of the ADRE variance with relative error within 10%, in these assessments. The results demonstrate the spectral dependencies of stratospheric ADRE and highlight the distinct radiative sensitivity of stratospheric aerosols, which differs significantly from that of tropospheric aerosols.

Hosted file

`manuscript_20240806.docx` available at https://authorea.com/users/632121/articles/1215182-quantifying-the-direct-radiative-effect-of-stratospheric-aerosols-using-radiative-kernels

Quantifying the Direct Radiative Effect of Stratospheric Aerosols Using Radiative Kernels

Qiurun Yu[1], Yi Huang[1]

[1] Department of Atmospheric and Oceanic Sciences, McGill University, Montreal, Quebec, Canada.

Corresponding author: Qiurun Yu (qiurun.yu@mail.mcgill.ca)

Key Points:

- A global dataset of radiative sensitivity kernels is developed to quantify stratospheric aerosol direct radiative effect (ADRE).
- An analytical model is developed to emulate the kernel values from a handful of predictor variables.
- The stratospheric aerosol kernels capture the spatiotemporally varying ADRE values of volcanic eruptions and wildfire events well.

Abstract

To facilitate the quantification of the stratospheric aerosol radiative effect, this study generates a set of aerosol direct radiative effect (ADRE) kernels based on MERRA-2 reanalysis data. These radiative kernels measure the sensitivities of ADRE to perturbations in scattering and absorbing aerosol optical depth (AOD), respectively. Both broadband and band-by-band radiative kernels are developed to account for the wavelength dependency of ADRE. The broadband kernels are then emulated by a multivariate regression model, which predicts the kernel values from a handful of predictors, including the top-of-atmosphere (TOA) insolation, TOA reflectance, and stratospheric AOD. These kernels offer an efficient and versatile way to assess the ADRE of stratospheric aerosols. The ADREs of the 2022 Hunga volcano eruption and the 2020 Australia wildfire are estimated from the kernels and validated against radiative transfer model-calculated results. The Hunga eruption induced a global mean cooling forcing of -0.46 W/m² throughout 2022, while the Australia wildfire caused a warming forcing of +0.28 W/m² from January to August. The kernel estimation can capture over 90% of the ADRE variance with relative error within 10%, in these assessments. The results demonstrate the spectral dependencies of stratospheric ADRE and highlight the distinct radiative sensitivity of stratospheric aerosols, which differs significantly from that of tropospheric aerosols.

Plain Language Summary

Stratospheric aerosols influence the Earth's energy balance by scattering and absorbing solar radiation, making it crucial to accurately measure their radiative impact. However, quantifying the aerosol radiative impact is computationally expensive if using radiative transfer models. In this work, we develop a set of aerosol radiative kernels, which can provide a flexible and efficient means for calculating the radiative effects of stratospheric aerosols. The kernels have been demonstrated to effectively quantify the radiative impacts of stratospheric aerosols resulting from wildfire and volcanic eruption events.

1 Introduction

Stratospheric aerosols influence the Earth's radiative energy budget and have profound climate impacts (Kremser et al., 2016). The largest contributor to stratospheric aerosols is volcanic eruptions, which can inject a mixture of sulfur dioxide, sulfuric acid, and water directly into the stratosphere, where they transform into stratospheric aerosols (Martinsson et al., 2019). By increasing the reflection of solar radiation, those volcanic aerosols exert a negative radiative forcing at the top-of-the-atmosphere (TOA), which can lead to pronounced surface cooling and changes in atmospheric circulation and water cycle (Robock, 2000; Grinsted et al., 2007; Wu et al., 2023; Günther et al., 2024). Apart from volcanic eruptions, wildfires-induced pyrocumulonimbus (PyroCb) events can also transport a significant amount of carbonaceous aerosols into the lower stratosphere (Fromm et al., 2010; Ohneiser et al., 2020; Liu et al., 2022; Damany-Pearce et al., 2022). Observation and model studies suggest that the absorptivity of biomass-burning aerosols can warm the stratosphere, deplete the stratospheric ozone, and modify vertical dynamics and horizontal dispersion (Damany-Pearce et al., 2022; Ohneiser et al., 2020, 2023).

Although the importance of stratospheric aerosols is well recognized, the quantification of their radiative effect has not been an easy task, as it requires the consideration of multiple factors, including aerosol types, height and size distributions, as well as the environmental factors at their locations (Weisenstein et al., 2015; MacMartin et al., 2017; Q.-R. Yu et al., 2019; Visioni et al., 2020; P. Yu et al., 2023; Q. Yu et al., 2024). The straightforward and most accurate way to quantify the aerosol direct radiative effect (ADRE) is the Partial Radiative Perturbation (PRP) method, which requires running a radiative transfer model and differencing the modeled radiative fluxes with and without aerosol perturbations, although this quantification method is computationally expensive. Many studies used alternative approaches to estimate ADRE, for example, by using an analytical relationship between the aerosol optical depth (AOD) and the radiative effect. Hansen et al. (2005) estimated a radiative sensitivity of -22 W/m^2 per unit AOD change, based on the simulation of the Pinatubo eruption case using a global climate model. P. Yu et al. (2023) reported a similar scaling relation for stratospheric aerosols also based on modeling experiments. (Schoeberl et al., 2023, 2024a) applied the radiative sensitivity kernels of Q. Yu & Huang (2023b) to evaluate the climate impacts of the 2022 Hunga volcano eruption. However, these kernels were derived based on the aerosol perturbations in the whole atmospheric column, which is dominated by tropospheric, as opposed to stratospheric aerosols.

To the best of our knowledge, a global dataset of radiative sensitivity kernels specifically developed for assessing the ADRE of stratospheric aerosols is still lacking. The existing global aerosol kernels, including those of Q. Yu & Huang, (2023b) and Thorsen et al. (2020), were developed with a focus on tropospheric aerosols, whose radiative sensitivity, as shown later in this paper, differ markedly from stratospheric aerosols. A recent study by Gao et al. (2023) tested the kernel quantification of the ADRE of tropopause aerosols, although the development was limited to the East Asia region. A global kernel dataset, which can facilitate an efficient yet accurate quantification of the spatiotemporally varying radiative impacts of stratospheric aerosols, is expected to have a broad spectrum of applications. This is especially relevant given the frequent occurrence of wildfires (Damany-Pearce et al., 2022), recent volcanic eruptions (Taha et al., 2022), and the increasing discussions about stratospheric aerosol geoengineering (Visioni et al., 2020).

It is well recognized that the aerosol optical properties, radiative transfer, and the resulting aerosol radiative effects, all have a strong spectral dependence. For example, the spectral dependence of AOD is often approximated using the Angstrom relationship (Ångström, 1929), although the Angstrom exponent (AE) may vary with wavelength (Schuster et al., 2006) and height (Chen et al., 2020). Incorporating spectrally measured aerosol optical properties can reduce uncertainty in the ADRE quantification (Chauvigné et al., 2021). Thorsen et al. (2020) found that distinguishing column-integrated aerosol optical properties in the mid-visible and near-infrared wavelengths can help constrain ADRE, pointing to the potential benefits of developing band-by-band kernels. In addition, spectral kernels may take advantage of the spectral AOD information, which is available from many state-of-the-art climate models as well as satellite and ground-based measurements. Therefore, in addition to a set of broadband stratospheric aerosol kernels, we also aim to produce an accompanying set of spectrally decomposed, band-by-band kernels, to facilitate the use of spectral information in the ADRE quantification.

Observational and modeling studies have shown that ADRE sensitivity is strongly influenced by environmental conditions such as clouds, relative humidity, and surface albedo (McComiskey et al., 2008; Loeb et al., 2019; Schoeberl et al., 2023; Q. Yu & Huang, 2023a, 2023b). However, the primary environmental factors affecting stratospheric ADRE sensitivity and their underlying physics remain to be elucidated. Another objective of our study is to investigate this environmental dependence. Integrating a physical model with statistical analyses, we experiment with sorting the global aerosol kernels, which are conventionally computed on geographic grids (latitude, longitude, and calendar month), based on the geophysical variables that govern the kernel values according to radiative transfer physics. We aim to establish an analytical equation to capture the spatiotemporal variations of the kernel values. Such an analytical relation can be considered a physical (as opposed to geographical) kernel dataset and can be used for the ADRE quantification under arbitrary situations regardless of the geographic location, which potentially makes the kernels suitable for broader applications.

In summary, in this study, we aim to develop a set of radiative sensitivity kernels that are specifically designed for quantifying the stratospheric ADRE. The kernels developed here include both broadband and spectral band-by-band TOA flux kernels provided on conventional latitude-longitude-month grids, as well as physically sorted broadband kernels whose values are determined from analytical equations. The structure of this paper is as follows. Section 2 details the methods used to calculate both broadband and band-by-band kernels. Section 3 describes the development of physically sorted kernels. These aerosol kernels constitute a versatile means to quantify the stratospheric ADRE. We demonstrate the use and performance of these kernels by applying them to two cases: the 2022 Hunga volcanic eruption (Bourassa et al., 2023; Kloss et al., 2022; Taha et al., 2022) and the 2020 Australia wildfire (Ohneiser et al., 2020; Damany-Pearce et al., 2022; Sellitto et al., 2022) in Section 4. A summary is provided in Section 5.

2 Data and Methods

2.1 Stratospheric Aerosol Direct Radiative Effect

The stratospheric ADRE is calculated as the difference in net radiative fluxes at TOA with and without stratospheric aerosols:

$$\text{Stratos ADRE} = F^{net}(all\ aerosols) - F^{net}(no\ stratos\ aerosols) \qquad (1)$$

where $F^{net} = F^{\downarrow} - F^{\uparrow}$, with the downward flux $F^{\downarrow}$ being positive.

In this study, we focus on the shortwave stratospheric ADRE at the TOA under the all-sky condition. This is because the longwave ADRE is orders of magnitude smaller (Reddy et al., 2005; Heald et al., 2014; Balmes & Fu, 2021), and aerosol scattering is often neglected in the longwave schemes of radiative transfer models (Mlawer et al., 1997, 2016), despite stratospheric aerosols being primarily scattering particles. However, the method described here can also be used to calculate aerosol kernels in the longwave spectrum, at the surface, or for atmospheric heating rate. Radiative fluxes are computed using the Rapid Radiative Transfer Model (RRTMG) (Mlawer et al., 1997, 2016). The required inputs for these calculations are obtained from the Modern-Era Retrospective Analysis for Research and Applications, Version 2 (MERRA-2) dataset (Gelaro et al., 2017). We use instantaneous atmospheric and cloud profiles, including air temperature and pressure, surface temperature, surface albedo, water vapor, ozone, specific humidity, cloud fraction, and the mass fraction of cloud liquid and ice water. The tropopause is defined according to the criterion of the World Meteorological Organization (WMO, 1957) as the lowest level where the temperature lapse rate decreases to 2 K/km or less, and the average lapse rate from this level to any level within the next 2 km does not exceed 2 K/km.

Aerosol optical properties are calculated based on the MERRA-2's instantaneous aerosol mixing ratio profiles, which include 72 layers. MERRA-2 provides 15 externally mixed aerosol tracers: hydrophobic and hydrophilic black and organic carbon, sulfate, dust (five size bins), and sea salt (five size bins) (Randles et al., 2017). Aerosol optical properties vary with relative humidity to account for hygroscopic growth. For computational efficiency, the 3-hourly MERRA-2 inputs are resampled into a 2.5° × 2.5° grid box. Our goal is to replicate the aerosol radiative transfer calculations from the MERRA-2 dataset and isolate the impact of stratospheric aerosols to study the stratospheric ADRE. Validations of aerosol optical property inputs and total ADRE calculations against MERRA-2 diagnostic aerosol and radiation products are provided in the Supporting Information (Figures S1-S3).

2.2 Computation of Stratospheric Aerosol Kernels

Aerosol radiative kernels ($\frac{\partial(ADRE)}{\partial x}$) are the partial derivative of the ADRE to an aerosol-related property x such as AOD and single scattering albedo. These kernels represent how ADRE responds to atmospheric aerosol perturbations. By multiplying the radiative kernels with the changes in x, we can approximate the resulting change in ADRE, which provides a convenient means for estimating the radiative impact of aerosols.

In this study, we develop kernels for both stratospheric scattering aerosol optical depth (AOD_{scat}) and absorbing aerosol optical depth (AOD_{abs}). For each type of kernel, radiative transfer calculations are performed twice: one with background aerosols and one with perturbations in the stratospheric aerosols. The sizes of the perturbation are 0.1 for AOD_{scat} and 0.01 for AOD_{abs} at 550 nm. The perturbation magnitude differs between stratospheric AOD_{scat} and AOD_{abs} due to the smaller background stratospheric AOD_{abs} compared to AOD_{scat}. We use absolute perturbation values instead of relative ones (such as 1%) to minimize noise from numerical errors caused by very small background AOD values. We have verified that the radiative flux changes respond linearly to the AOD perturbations within the typical magnitudes of stratospheric aerosol perturbations (ΔAOD_{scat} ranging from 10^{-3} to 1 and ΔAOD_{abs} ranging from 10^{-4} to 1, respectively). The sum of the AOD_{scat} and AOD_{abs} effects can also be linearly added to determine the total stratospheric ADRE. Sensitivity tests have also been conducted to determine the impacts of perturbation height on the aerosol kernels. Results indicate minimal difference between perturbing a single layer at random altitudes versus the entire stratosphere. Therefore, for our perturbation runs, we assume a conserved vertical profile shape of stratospheric aerosols. Details about sensitivity tests of linear scaling, linear additivity, and height dependency of stratospheric aerosol kernels are provided in the Supporting Information (Figures S4-S6).

The perturbation computations produce both broadband and band-by-band stratospheric aerosol kernels. To account for the diurnal cycle, the 3-hourly kernels are averaged into monthly mean values. These aerosol kernels are computed for an El Niño-Southern Oscillation (ENSO) neutral year, 2022. The impact of interannual variability on aerosol kernels is small, as demonstrated by the comparisons of monthly mean kernels between 2020 and 2022. The R-squared values and Root Mean Squared Errors (RMSE) between the monthly mean AOD_{scat} kernels in those two years are 92% and 3.62, respectively, while for the AOD_{abs} kernels, they are 97% and 46.90, respectively. Detailed comparisons are provided in the Supporting Information (Figure S7), showing consistency in both spatial distributions and global mean values.

2.2.1 Broadband Aerosol Kernels

Given that solar energy peaks in the mid-visible bands and that aerosol optical properties are commonly observed in this range, we use the 550 nm AOD as the perturbation variable. The stratospheric AOD_{scat} and AOD_{abs} kernels are defined as follows:

$$\frac{\partial(ADRE)}{\partial(AOD_{scat})} = \frac{F^{net}(AOD_{scat}+\Delta AOD_{scat},\ AOD_{abs}, \mathrm{SSA'}, \mathrm{g'}) - F^{net}(AOD_{scat},\ AOD_{abs},\ \mathrm{SSA}, \mathrm{g})}{\Delta AOD_{scat}^{550}} \quad (2)$$

$$\frac{\partial(ADRE)}{\partial(AOD_{abs})} = \frac{F^{net}(AOD_{sca},\ AOD_{abs}+\Delta AOD_{abs}, \mathrm{SSA'}, \mathrm{g'}) - F^{net}(AOD_{scat},\ AOD_{abs},\ \mathrm{SSA}, \mathrm{g})}{\Delta AOD_{abs}^{550}} \quad (3)$$

In the unperturbed runs, the background aerosol profiles of AOD, single scattering albedo (SSA), and asymmetry factor (g) are taken from reconstructed MERRA-2 aerosol optical property profiles. In the perturbation runs, an aerosol layer representing the stratospheric aerosol perturbations is added to the background aerosol profile. This added aerosol layer has the scattering or absorbing AOD values at 550 nm of 0.1 and 0.01, respectively, and the incremental AOD values (ΔAOD_{scat} and ΔAOD_{abs}) at other wavelengths are prescribed according to the Angstrom relationship (with the AE being 1). For the scattering AOD perturbation, the SSA and g values of this added layer are assumed to be 1 and 0.7. The g value is based on annual and global mean asymmetry factor values reported by Ayash et al. (2008) as well as the background upper troposphere and lower stratosphere aerosol configurations in Sellitto et al. (2022). Weighted averaging is used to calculate the values of these aerosol properties in the perturbation runs. For AOD_{scat} perturbation runs,

$$SSA' = \frac{SSA^{550}AOD^{550} + 1*\Delta AOD_{scat}^{550}}{AOD^{550} + \Delta AOD_{scat}^{550}} \quad (4)$$

$$g' = \frac{g^{550}SSA^{550}AOD^{550} + 0.7*1*\Delta AOD_{scat}^{550}}{SSA^{550}AOD^{550} + 1*\Delta AOD_{scat}^{550}} \quad (5)$$

For AOD_{abs} perturbation runs, the SSA and g values are

$$SSA' = \frac{SSA^{550}AOD^{550} + 0*\Delta AOD_{abs}^{550}}{AOD^{550} + \Delta AOD_{abs}^{550}} \quad (6)$$

$$g' = g \quad (7)$$

To use the aerosol kernels derived here to calculate ADRE, users simply need to obtain stratospheric ΔAOD_{scat}^{550} and ΔAOD_{abs}^{550} values appropriate to the case of interest, and then multiply these with broadband kernel values.

$$\Delta ADRE = \frac{\partial(ADRE)}{\partial(AOD_{scat})} \cdot \Delta AOD_{scat}^{550} + \frac{\partial(ADRE)}{\partial(AOD_{abs})} \cdot \Delta AOD_{abs}^{550} \quad (8)$$

Figure 1 shows the global distribution of annual mean stratospheric AOD_{scat} and AOD_{abs} kernels, in the units of W/m^2 per unit change in stratospheric AOD. Both AOD_{scat} and AOD_{abs} kernels exhibit strong atmosphere dependencies. In cloudy regions (e.g., the Intertropical Convergence Zone, tropical eastern Atlantic, northwest Pacific Ocean, and Southern Ocean), the sensitivity of stratospheric ADRE to stratospheric AOD_{scat} is relatively lower due to the presence of underlying clouds, while the sensitivity to AOD_{abs} is relatively higher, compared to other regions. This is because in the case of the scattering effect, clouds already brighten the atmosphere and make the TOA radiation less sensitive to scattering aerosols and in the case of the absorbing effect, clouds increase the solar radiation reflected into the stratosphere, thereby amplifying the absorption by the stratospheric aerosols. Similar patterns are observed over the polar and desert regions with high surface albedo. Because of their scattering or absorbing nature, AOD_{scat} kernels are always negative, while AOD_{abs} kernels are always positive. In terms of global means, a 0.1 increase in stratospheric AOD_{scat}^{550} results in a -2.65 W/m² cooling, while a 0.1 increase in AOD_{abs}^{550} results in a +41.95 W/m² warming at the TOA. Note that these sensitivity values are larger than those reported by Q. Yu & Huang (2023b), particularly for absorbing aerosols. This is because the kernels developed in this study focus exclusively on stratospheric aerosols. These aerosols interact with a larger proportion of photons that have not been attenuated by clouds or tropospheric absorbers. Additionally, underlying clouds enhance the brightness of the troposphere, which further intensify the sensitivity of stratospheric ADRE to AOD_{abs}.

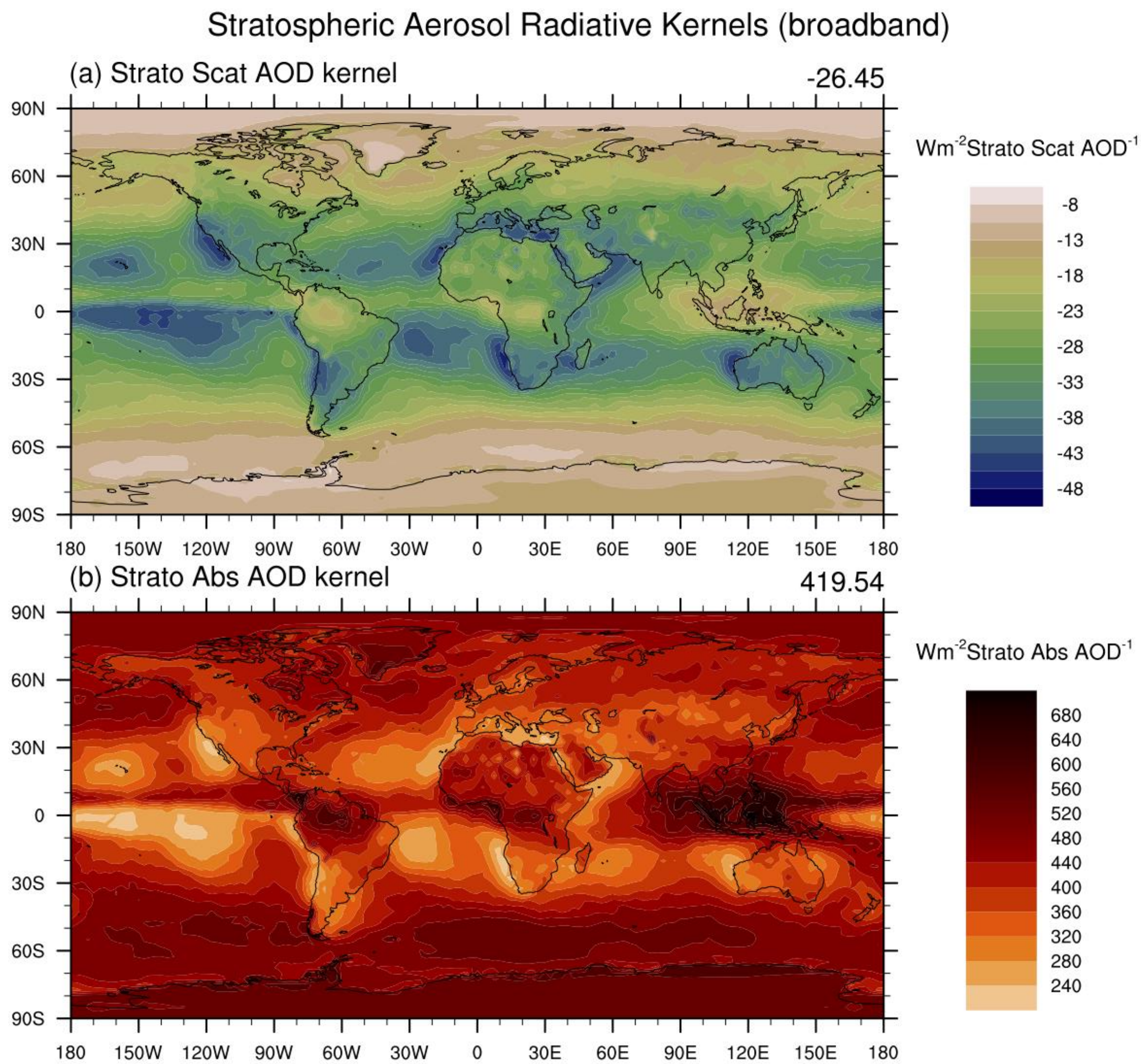

Figure 1. Spatial distributions of annual mean broadband aerosol kernels (a) for stratospheric AOD_{scat} and (b) for stratospheric AOD_{abs}. The global mean and annual mean values are indicated in the upper right corner of each subplot. Kernels are shown in units of watts per square meter per unit change in stratospheric AOD at 550 nm.

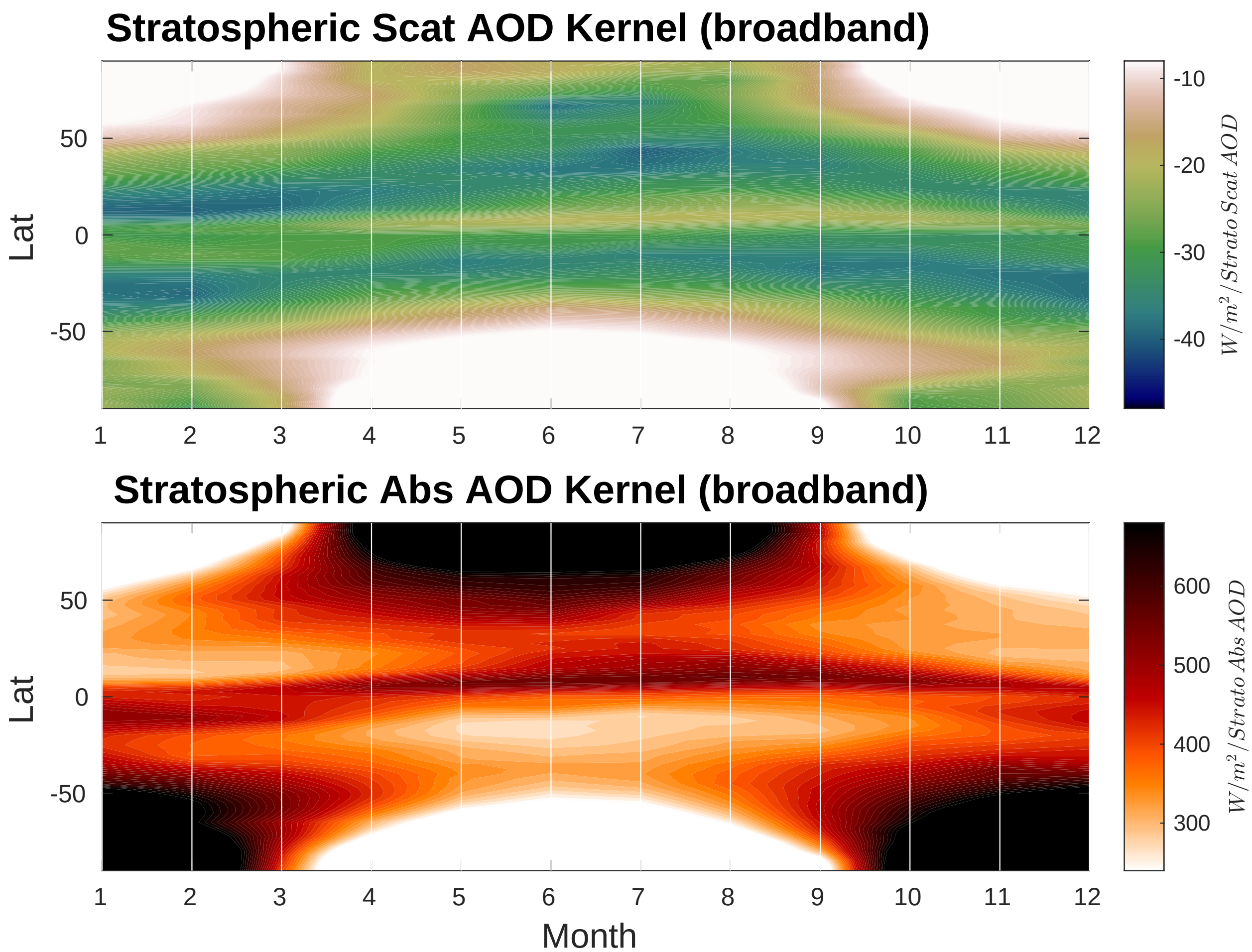

Figure 2. Temporal variations of zonal mean broadband stratospheric aerosol kernels (a) for stratospheric AOD_{scat} and (b) for stratospheric AOD_{abs}.

Apart from the spatial inhomogeneity, stratospheric aerosol kernels also display strong temporal variations. Figure 2 displays the temporal variations in zonal mean stratospheric broadband AOD_{scat} and AOD_{abs} kernels. The pronounced latitudinal differences in aerosol kernels reflect patterns of solar insolation. In tropical regions, the sensitivity of ADRE to stratospheric aerosols remains high throughout the year, while polar regions show notable seasonal variations.

2.2.2 Band-by-band Aerosol Kernels

While broadband aerosol kernels are convenient to use, they rely on assumptions about the wavelength dependency of aerosol optical properties, which may not always be accurate. To facilitate a more flexible and accurate ADRE quantification, we leverage the band configuration of the RRTMG model to calculate a set of band-by-band stratospheric aerosol kernels. The RRTMG shortwave bands, detailed in Table 1, cover a spectrum from 0.2 µm to 12.2 µm across 14 bands.

Table 1. RRTMG shortwave bands.

SW band	**Wavenumber** $\boldsymbol{v[cm^{-1}]}$	**Wavelength** $\boldsymbol{\lambda\ [nm]}$	**AOD wavelength [nm]**
Band 29	820-2600	12195- 3846	7082.2
Band 16	2600-3250	3846-3077	3444.7
Band 17	3250-4000	3077-2500	2777
Band 18	4000-4650	2500-2151	2320.2
Band 19	4650-5150	2151-1942	2044.2
Band 20	5150-6150	1942-1626	1778.4
Band 21	6150-7700	1626-1299	1455.2
Band 22	7700-8050	1299-1242	1270
Band 23	8050-12850	1242-778	944.3
Band 24	12850-16000	778-625	693.5
Band 25	16000-22650	625-442	527.1
Band 26	22650-29000	442-345	399.8
Band 27	29000-38000	345-263	329.1
Band 28	38000-50000	263-200	229.8

The stratospheric aerosol band-by-band kernels for AOD_{scat} and AOD_{abs} are expressed as:

$$\frac{\partial ADRE^i}{\partial AOD^i_{scat}} = \frac{F^{net}(AOD^i_{scat}+\Delta AOD^i_{scat}, AOD^i_{abs}, \mathrm{SSA}', \mathrm{g}') - F^{net}(AOD^i_{scat}, AOD^i_{abs}, \mathrm{SSA}^i, \mathrm{g}^i)}{\Delta AOD^i_{scat}} \quad (9)$$

$$\frac{\partial ADRE^{i}}{\partial AOD_{abs}^{i}} = \frac{F^{net}(AOD_{scat}^{i}, AOD_{abs}^{i}+\Delta AOD_{abs}^{i}, \text{SSA}', \text{g}') - F^{net}(AOD_{scat}^{i}, AOD_{abs}^{i}, \text{SSA}', \text{g}')}{\Delta AOD_{abs}^{i}} \quad (10)$$

In the equations above, i represents the i[th] band in RRTMG. ΔAOD_{scat}^{i} and ΔAOD_{abs}^{i} are the added AOD perturbation at the i[th] band, which vary with wavelength according to the Angstrom relation in our calculation.

$$\Delta AOD_{scat}^{i} = 0.1 * \left(\frac{wavelength^{i}}{550}\right)^{-1} \quad (11)$$

$$\Delta AOD_{abs}^{i} = 0.01 * \left(\frac{wavelength^{i}}{550}\right)^{-1} \quad (12)$$

Note that for each band, perturbed AOD is calculated at the central wavelength following RRTMG configuration as listed in Table 1. The SSA and g calculations in the perturbation runs are similar to those in the broadband kernel calculation.

To use the band-by-band kernels, users need to obtain the ΔAOD_{scat}^{i} and ΔAOD_{abs}^{i} for each band, multiply them by band-by-band kernels, and sum over the 14 bands.

$$\Delta\text{ADRE} = \sum_{i=16}^{29}\left(\frac{\partial ADRE^{i}}{\partial AOD_{scat}^{i}} \cdot \Delta AOD_{scat}^{i}\right) + \sum_{i=16}^{29}\left(\frac{\partial ADRE^{i}}{\partial AOD_{abs}^{i}} \cdot \Delta AOD_{abs}^{i}\right) \quad (13)$$

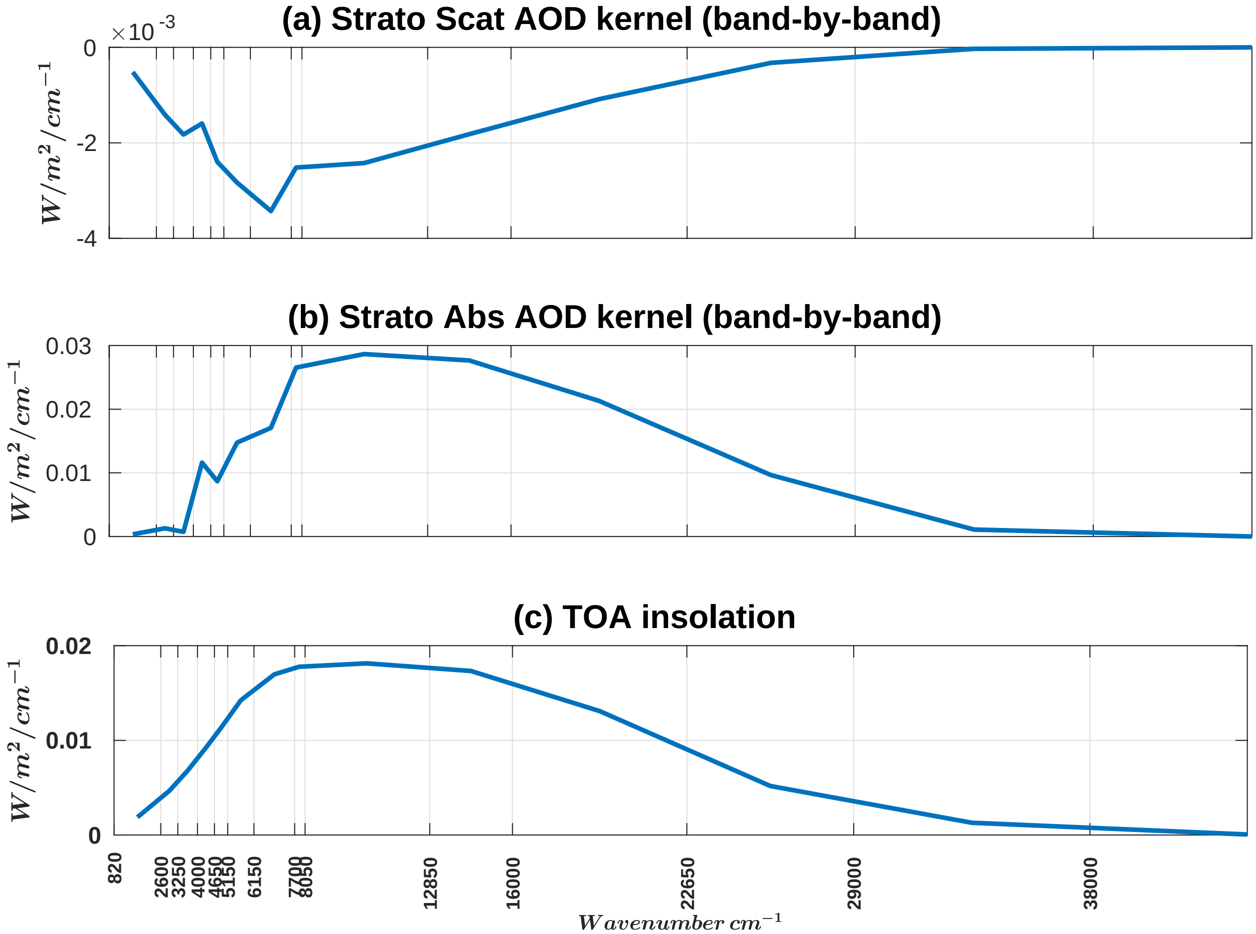

Figure 3. Global mean annual mean stratospheric aerosol band-by-band kernels for (a) AOD_{scat} and (b) AOD_{abs}. For demonstration purposes, kernels are normalized by the corresponding bandwidth. The normalized kernel unit is watts per meter squared per unit change in the respective stratospheric AOD per wavenumber. (c) Normalized spectral solar radiation.

Figure 3 presents the global mean band-by-band stratospheric AOD_{scat} and AOD_{abs} kernels. For comparison purposes, the spectral kernels are normalized by the bandwidth. The results indicate that the spectral signatures of the band-by-band aerosol kernels are primarily dominated by the strength of incoming solar radiation. The aerosol radiative sensitivity peaks from the near-ultraviolet band (~22650 cm^{-1}) to the near-infrared band (~8080 cm^{-1}), which corresponds to band 23 to 25 (442 nm-1242 nm) in RRTMG as indicated in Table 1. Accurately determining aerosol optical properties in these bands can help constrain the ADRE without needing the aerosol information across the full spectrum. Most aerosol retrieval products provide optical properties at a few discrete wavelengths ranging from near-ultraviolet to near-infrared. For example, the AErosol RObotic NETwork (AERONET) provides AOD products at 340, 380, 440, 500, 675, 870, and 1020 nm (Giles et al., 2019). By interpolating observed AOD values at the central AOD wavelengths in the RRTMG configuration for relevant bands and assuming spectral dependence of optical properties for the remaining bands, users can calculate stratospheric ADRE more accurately than using broadband kernels. In the following section, we will use the spectral AOD observations to compare the ADRE values computed from the broadband and band-by-band stratospheric aerosol kernels.

2.3 OMPS Aerosol Data and Quality Control

To quantify the stratospheric ADRE, we utilize the aerosol extinction coefficient profiles from the OMPS-LP Level 2 daily product. The Ozone Mapping and Profiler Suite (OMPS) measures limb scattering of sunlight at tangent altitudes from ground level up to approximately 100 km with a vertical resolution of 1km (Flynn et al., 2006). The aerosol product from OMPS has been widely used to study the stratospheric ADRE (Damany-Pearce et al., 2022; Bourassa et al., 2023; Schoeberl et al., 2023, 2024). This study uses aerosol extinction coefficient retrievals along the center slit (aligned with the orbital track) of the OMPS-LP. The retrieved extinction profiles extend up to 40km, and quality control procedures are applied before the analysis following Damany-Pearce et al. (2022). Only data with ResidualFlag = 0, SingleScatteringAngle $\leq 145^\circ$, and SwathLevelQualityFlags with bits 0, 1, and 7 = 0 are considered valid. The tropopause definition is consistent with that used in the kernel calculation. We integrate the extinction coefficient throughout the stratosphere to calculate the stratospheric AOD. To facilitate kernel application, we average the AOD data onto the same $2.5° \times 2.5°$ latitude-longitude grid.

For using the broadband aerosol kernels, we choose the 869 nm extinction coefficient from OMPS and scale it to 550 nm, assuming an AE value of 1. This AE value is chosen because it represents the background stratospheric aerosol conditions and the specific conditions of the Hunga aerosols, and has been applied in other similar studies (Schoeberl et al., 2023; Sellitto et al., 2024). The 869 nm wavelength is chosen over other channels closer to 550 nm because OMPS aerosol products have performance issues at shorter wavelengths in the southern hemisphere (Taha et al., 2021).

For the band-by-band kernel application, we utilize extinction coefficients measured at 510 nm, 600 nm, 675 nm, 745 nm, 869 nm, and 997 nm, and interpolate extinction values to 527.1 nm, 693.5 nm, and 944.3 nm using measurements from the nearest wavelengths as required by the aerosol kernels. For the remaining bands, we scale the extinction coefficient from 869 nm to the corresponding central AOD wavelength, assuming an AE of 1. In the following section, we use the OMPS spectral AODs as an example to demonstrate the usage of our kernels.

Our goal is to estimate the changes in stratospheric ADRE (ΔADRE) due to the 2022 Hunga volcanic eruption and the 2020 Australia wildfires using our aerosol kernels. We consider the MERRA-2 stratospheric AOD as the background aerosol states because no eruptive volcanoes are included in MERRA-2 after 2010 (Randal et al., 2016). Therefore, the stratospheric AOD anomaly is calculated by subtracting the background stratospheric AOD values given by MERRA-2 from OMPS stratospheric AOD. For the kernel application, the AOD values in Equations (8) and (13) are the differences between OMPS and MERRA-2 stratospheric AOD. To validate the performance of our aerosol kernels, we use the same AOD anomalies as input to the RRMTG model to calculate the "truth" values of stratospheric ADRE for comparison.

3 Physically Sorted Aerosol Kernels

As shown in the previous section (e.g., Figures 1 and 2), there are strong spatial and temporal variabilities in the kernel values. It is thus important to understand how the aerosol properties and environmental variables (e.g., surface albedo and clouds) interact with each other to influence the radiative sensitivity. To address this question, we follow a widely used conceptual model of ADRE (Chlek & Coakley Jr, 1974; Haywood & Shine, 1995) to identify the key factors and their expressions to use in an analytical model to predict the kernel values. We then determine the coefficient values statistically using a multivariable regression method following (Q. Yu & Huang, 2023a, 2023b). Different from the geographically gridded kernels presented in the previous section, the physically sorted kernels developed here are not constrained by space and time, allowing one to more flexibly estimate the stratospheric ADRE.

3.1 Physical Model

We follow the formulation of Haywood & Shine (1995), but consider the stratospheric aerosols as a scattering layer and represent the troposphere-surface system as a whole with a reflectance parameter at the tropopause. The all-sky stratospheric ADRE at the TOA can be expressed as follows:

$$\mathrm{ADRE} = -\mathrm{S}T_{\mathrm{at}}^{2}\beta\omega\tau\sec\theta\,\frac{(1-R_s)^2-\frac{R_s(1-\omega)}{\beta}\left[\frac{2-\tau\sec\theta}{\omega}-\tau\sec\theta(2\beta-1)\right]}{1-R_s\beta\omega\tau\sec\theta} \quad (14)$$

The environment-related variables are solar insolation (S), atmospheric transmittance (T_{at}) above the aerosol layer, the solar zenith angle (θ), and tropopause reflectance (R_s). The aerosol-related variables are the aerosol backscattering ratio (β), aerosol single scattering albedo (ω), and aerosol optical depth (τ). The stratospheric ADRE is further expanded as:

$$\mathrm{ADRE} = -\mathrm{S}T_{\mathrm{at}}^{2}\beta\omega\tau\sec\theta(1+R_s\tau\sec\theta\beta\omega)\left\{(1-R_s)^2-\frac{R_s(1-\omega)}{\beta}\left[\frac{2-\tau\sec\theta}{\omega}-\tau\sec\theta(2\beta-1)\right]\right\} \quad (15)$$

The sensitivity of stratospheric ADRE to τ is

$$\frac{\partial ADRE}{\partial\tau} = -\mathrm{S}T_{\mathrm{at}}^{2}\beta\omega(1-R_s)^2(1+2\beta\omega R_s\tau\sec\theta)+\mathrm{S}T_{\mathrm{at}}^{2}\beta\omega(1+2\beta\omega R_s\tau\sec\theta)\frac{R_s(1-\omega)}{\beta}\left[\frac{2-\tau\sec\theta}{\omega}-\tau\sec\theta(2\beta-1)\right]+\mathrm{S}T_{\mathrm{at}}^{2}\beta\omega(\tau\sec\theta+\beta\omega R_s\tau\sec\theta^2)\left[-\frac{R_s}{\beta}\frac{1-\omega}{\omega}-2\beta+1\right] \quad (16)$$

Neglecting higher-order terms, Equation (16) is approximated as

$$\frac{\partial ADRE}{\partial\tau} = -\mathrm{S}T_{\mathrm{at}}^{2}[\beta\omega+R_s(2\beta\omega+2-3\omega)-R_s^2\beta\omega+R_s\tau\sec\theta(-2+3\omega-2\omega\beta-\omega^2)+\beta\omega\tau\sec\theta] \quad (17)$$

This equation suggests that stratospheric aerosol kernels are influenced by these terms: R_s, $R_s\tau$, τ, and R_s^2. The combination terms arise from the coupling effects between the stratospheric aerosol layer and the underlying troposphere-surface system. In the following section, we will use these terms as predictors to reproduce the spatiotemporally varying stratospheric aerosol kernels. The goal is to capture the physical processes governing ADRE sensitivity, which should be independent from geographic locations.

3.2 Statistical Model

Regression models have been a useful tool in predicting radiative forcing and capturing nonlinear radiative interactions in many studies (Huang et al., 2016; Datseris et al., 2022; Q. Yu & Huang, 2023b, 2023a). In this work, we built a multi-variable regression model to represent the annual mean global stratospheric aerosol kernels following Q. Yu & Huang (2023b, 2023a). The model is expressed as:

$$\frac{\mathbf{Y(i,j)}-\overline{\mathbf{Y}}}{\overline{\mathbf{Y}}} = \sum_{\mathbf{k=1}}^{\mathbf{n}}\mathbf{A_k}\frac{\mathbf{X_k(i,j)}-\overline{\mathbf{X_k}}}{\overline{\mathbf{X_k}}} \quad (18)$$

Here, X are predictors (e.g., R_s, $R_s\tau$) at latitude i and longitude j. Y is either the broadband aerosol kernels for stratospheric AOD_{scat} or AOD_{abs}. A_k is the regression coefficient and n is the number of predictors. Note that the global field of Y is predicted by one uniform set of A_k values. Both predictors and predictands are normalized by their global mean values, denoted by a bar.

Following the physical model derived above, we select R_s, $R_s\tau$, τ, and R_s^2 as predictors. As TOA reflectance (R) is more easily obtained, we use it as a proxy for the tropopause reflectance. To accurately represent global aerosol kernels using as few predictors as possible, we have tested the performance of all possible combinations of predictors (listed in Supporting Information Table 1&2). Results suggest that the four predictors are sufficient to capture almost all main features of stratospheric aerosol kernels.

The physically sorted broadband aerosol kernels for stratospheric AOD_{scat} is given by

$$\frac{\frac{\frac{\partial(ADRE)}{\partial(AOD_{scat})}}{S}-(-0.076)}{(-0.076)} = -2.264 \cdot \frac{R-0.413}{0.413} + 0.753\frac{R^2-0.184}{0.184} + 0.671\frac{\tau-0.002}{0.002} - 0.3186\frac{R\tau-0.001}{0.001} \quad (19)$$

The physically sorted broadband aerosol kernels for stratospheric AOD_{abs} is given by

$$\frac{\frac{\frac{\partial(ADRE)}{\partial(AOD_{abs})}}{S}-1.323}{1.323} = -0.313 \cdot \frac{R-0.413}{0.413} + 0.696\frac{R^2-0.184}{0.184} - 0.175\frac{\tau-0.002}{0.002} + 0.258\frac{R\tau-0.001}{0.001} \quad (20)$$

The comparison of statistically fitted broadband aerosol kernels for stratospheric AOD_{scat} and AOD_{abs} against benchmark RRTMG calculations is shown in the Supporting Information (Figures S8). Results suggest that more than 94% of the spatial variance in aerosol kernels is captured by the regression model, indicating its effectiveness in predicting the variability of aerosol kernels.

Figure 4 displays the impact of environmental variables (TOA insolation S and reflectance R) on the distributions of annual mean global aerosol kernels. Generally speaking, an increase in solar insolation results in a larger magnitude of aerosol kernels, while a more reflective underlying "surface" (due to clouds or Earth's surface) leads to a less cooling or more warming impact on net TOA fluxes. The physically sorted aerosol kernels can well capture their sensitivity to those environmental variables. More importantly, they can estimate stratospheric ADRE sensitivity in idealized conditions where actual observations are lacking.

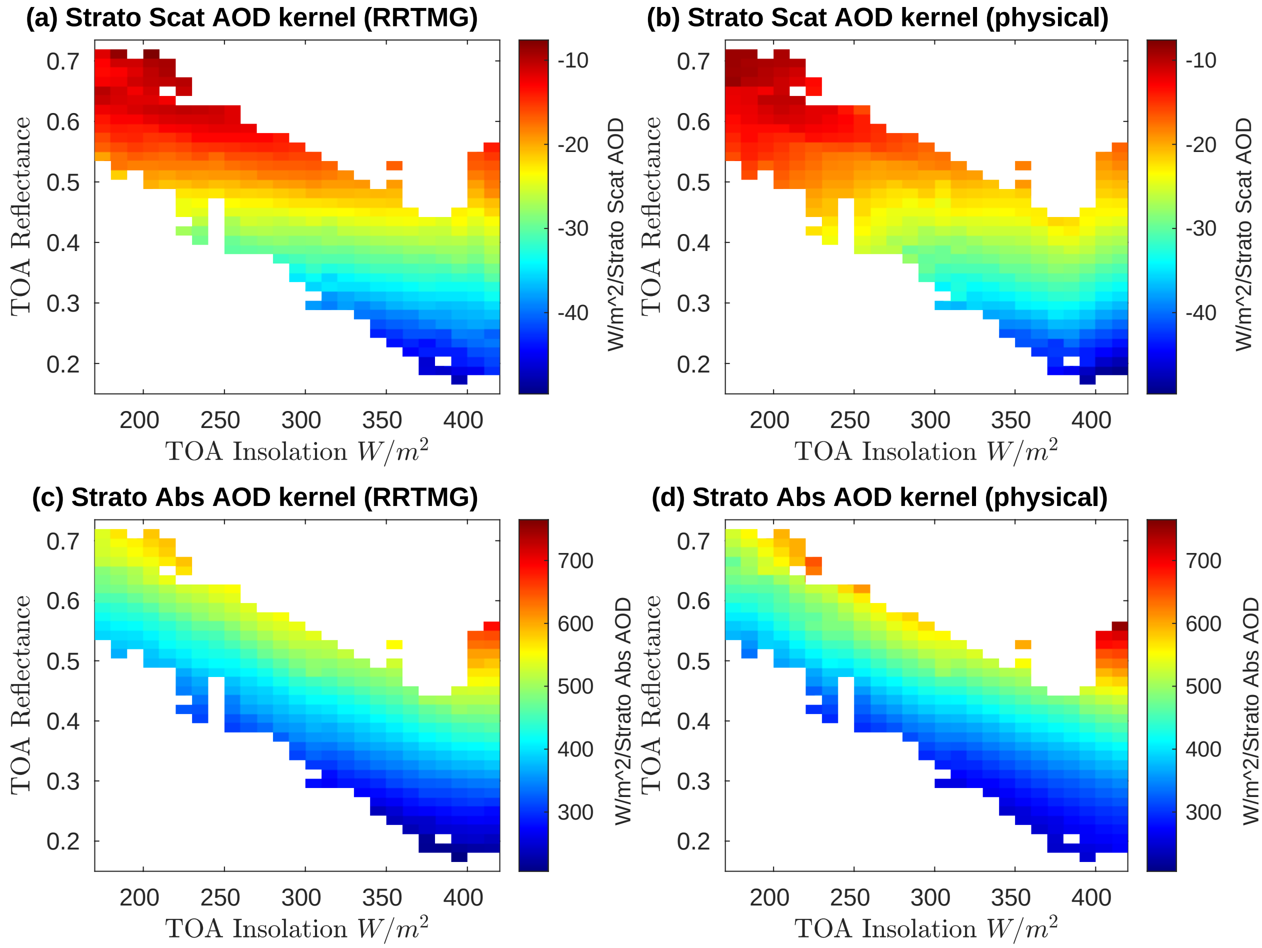

Figure 4. Distributions of broadband stratospheric AOD_{scat} and AOD_{abs} kernels as a function of TOA reflectance and TOA insolation. Left column: RRTMG-calculated stratospheric aerosol kernels; Right column: the physically sorted aerosol kernels predicted by the regression model.

4 Stratospheric Aerosol Kernel Applications

Multiplying aerosol radiative kernels by changes in stratospheric AOD from specific events (e.g., volcanic eruptions) provides estimates of the corresponding ADRE. In this section, we examine the radiative effects of the volcanic ash plume from the 2022 Hunga eruption and the biomass-burning aerosols from the 2020 Australia wildfires to demonstrate the application of stratospheric aerosol kernels. We compare the results of broadband, band-by-band, and physically sorted kernels.

4.1 Aerosol Radiative Kernel Comparisons

Given the kernels here are developed specifically for stratospheric aerosols, it is of interest to compare them with other kernels not designed this way. Besides the simple scaling relations given in the literature (e.g., Hansen et al. 2005; P. Yu et al. 2021), Q. Yu & Huang, (2023b, denoted as YH23 from here on) derived a set of global ADRE sensitivity kernels mainly for tropospheric aerosols and validated against the independent results of Thorsen et al. (2020).

Schoeberl et al. (2023, 2024) used the YH23 kernels to estimate the radiative impact of the Hunga eruption. We include the YH23 kernels for comparison in the following.

In Figure 5, we compare the zonal mean AOD_{scat} and AOD_{abs} sensitivity in YH23 with the broadband stratospheric aerosol kernels calculated by RRTMG and the statistical regression model. Results show that the aerosol kernels display significant latitudinal differences. For all-sky stratospheric AOD_{scat} kernels, the magnitude peaks in the subtropical regions because the relative brightness of aerosols is reduced above the tropical cloudy regions. The physically sorted kernels closely match the RRTMG results, indicating a good performance of the physical sorting method. Interestingly, the clear-sky, as opposed to the all-sky, AOD_{scat} kernels given by YH23 render more similar magnitudes to the all-sky stratospheric AOD_{scat} kernels developed here, especially in the mid-latitudes. This is because the stratospheric aerosols are located above tropospheric clouds, which suppress the radiative sensitivity to tropospheric AOD perturbations but do not strongly affect the radiative effect of stratospheric aerosols. Compared to the AOD_{abs} kernels in YH23, the stratospheric AOD_{abs} kernels developed here are much larger due to the enhanced ADRE sensitivity to AOD_{abs} above bright underlying clouds.

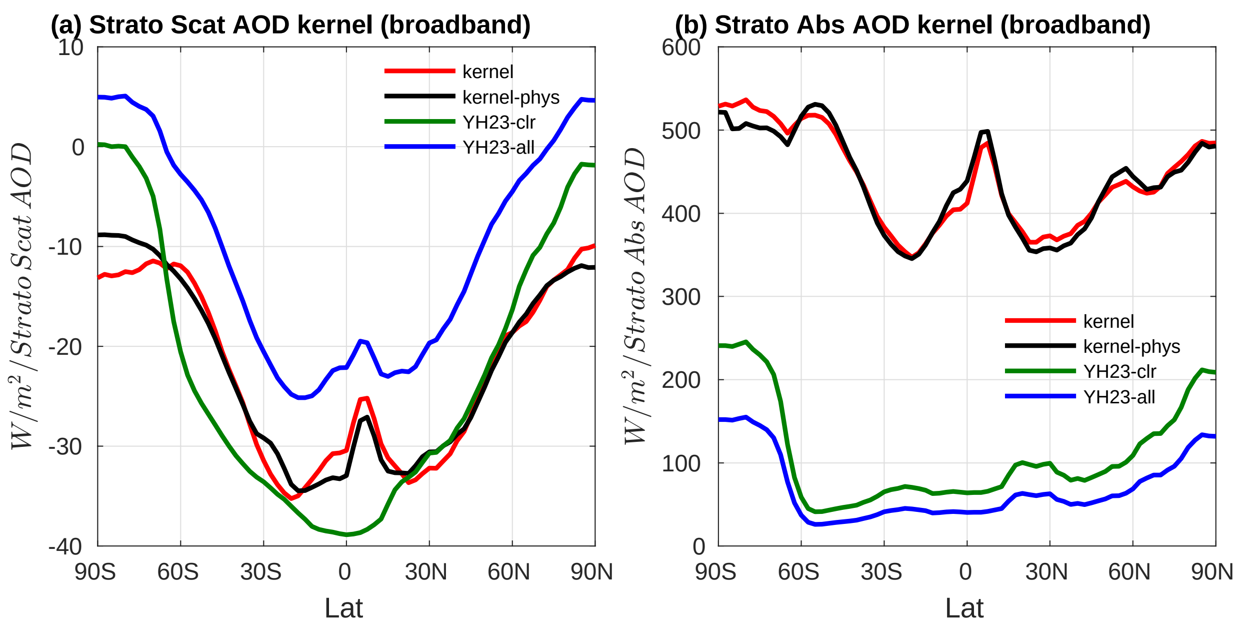

Figure 5. Annual mean and zonal mean broadband stratospheric (a) AOD_{scat} and (b) AOD_{abs} radiative kernels. YH23-clr and YH23-all represent the clear-sky and all-sky scattering AOD radiative sensitivity quantified in Q. Yu & Huang (2023b) for tropospheric aerosols. Kernel and Kernel-phys indicate the broadband kernels calculated from RRTMG and emulated by a regression model, respectively.

4.2 2022 Hunga Volcanic Eruption

On January 15, 2022, the Hunga Tonga volcano (20.57°S, 175.38°W) erupted violently, releasing sulfur compounds and other aerosols into the atmosphere (Kloss et al., 2022; Taha et al., 2022; Schoeberl et al., 2023, 2024). To assess the corresponding ADRE, we first calculate the stratospheric AOD anomaly following Section 2.3.

Figure 6a-6d shows the evolution of the zonal mean stratospheric AOD anomaly relative to the background at different wavelengths throughout 2022. Although the Hunga eruption occurred in late January, the OMPS product showed little AOD signal initially because the extinction retrieval becomes unreliable in the presence of clouds and optically thick aerosol plumes (Taha et al., 2021). Over time, the aerosol plume descented to the lower stratosphere and dispersed horizontally. Within four months after the eruption, the aerosols primarily remained in tropical latitudes with some northward spread. This led to an initial AOD peak in the tropical regions due to the immediate formation and accumulation of aerosols, as reported by other studies (Schoeberl et al., 2023; Taha et al., 2022). As the southern hemisphere approached winter, a meridional circulation developed between the tropics and subtropics to maintain the thermal wind balance, known as the QBO direct, meridional, or secondary circulation (Strahan et al., 2015). This circulation transported stratospheric aerosols into the mid-latitudes. Meanwhile, the polar vortex acted as a barrier, causing the accumulated aerosols in the subtropics to create a second AOD peak during July-September. The double peak features shown here were also reported in other observations and model simulations (Wang et al., 2023; Schoeberl et al., 2024). Gaps in the data are caused by spacecraft anomalies or failures to meet the data screening criteria.

Figure 6e also suggests that the zonal average stratospheric AOD anomaly varies significantly with wavelength, indicating that assuming a simple Angstrom exponent cannot fully represent the wavelength dependency of AOD. Therefore, it is important to incorporate the band-by-band kernels with AOD observations to accurately calculate the stratospheric ADRE.

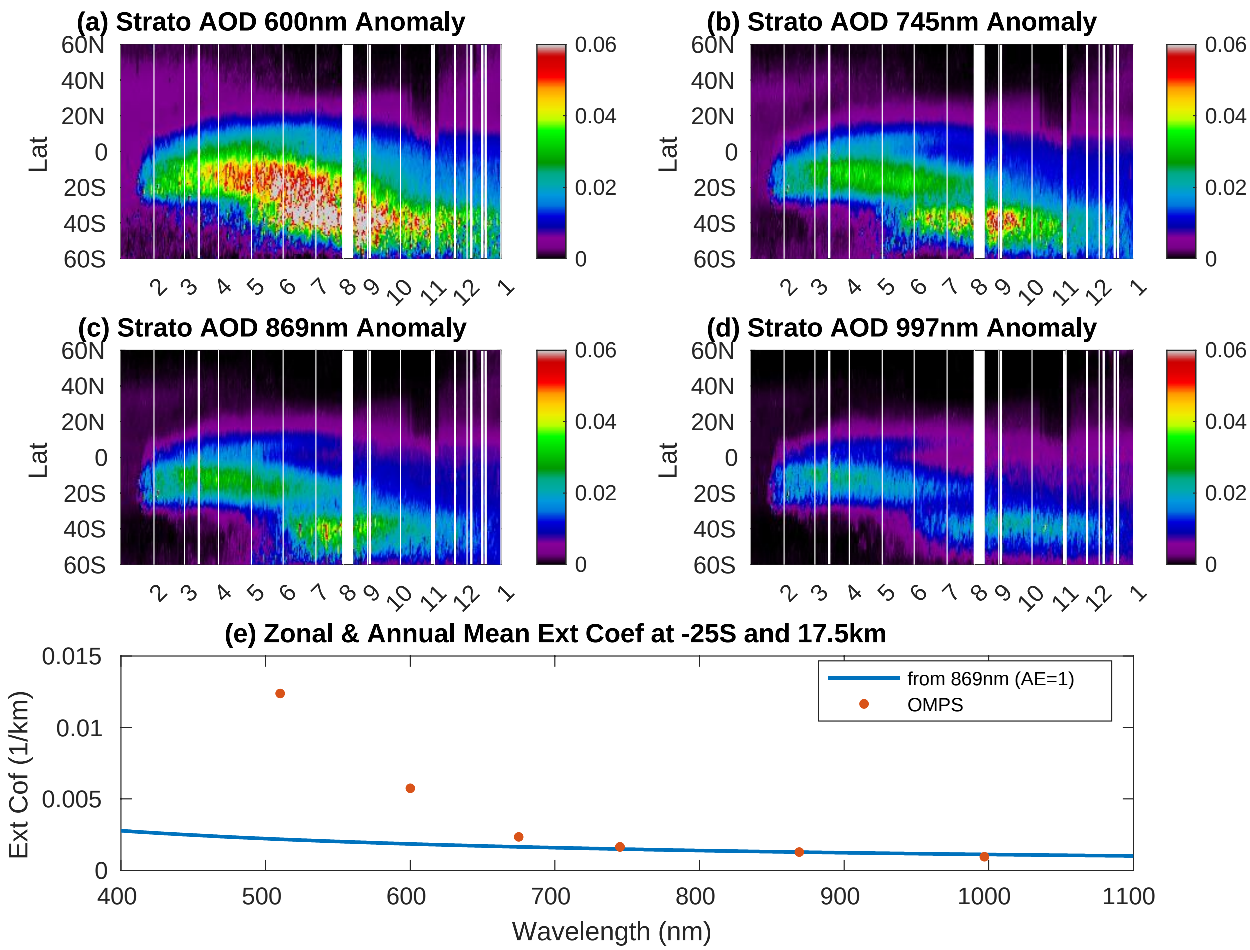

Figure 6. Latitude-time plots of the zonal mean stratospheric AOD anomaly at (a) 600 nm, (b) 745 nm, (c) 869 nm, and (d) 997 nm from OMPS-LP in 2022, with the x-axis in (a)-(d) representing corresponding months. (e) Zonal and annual mean aerosol extinction coefficient at -25S and 17.5 km. The red dots represent OMPS observations, while the blue line shows the wavelength dependency assuming an AE of 1.

In the ADRE calculation, we assume the AOD anomaly with SSA = 1 because observations suggest that the absorbing particles in the volcanic ashes are of small amounts and do not significantly impact the radiative properties (Kloss et al., 2022). We also assume the stratospheric AOD anomalies from OMPS at a discrete set of wavelengths represent the observational truth. Figure 7a displays the global mean stratospheric AOD anomaly as calculated in Section 2.3 throughout 2022. We have listed the spectral AOD anomaly at RRTMG mid-visible bands (bands 23-25). These values are interpolated from the nearby wavelengths from OMPS. For the broadband AOD anomaly, we calculate the AOD using OMPS 869 nm, assuming an AE of 1. This way, we can estimate the relative errors of the broadband kernel method when there are observation uncertainties in AE. Results indicate distinct features in the spectra AOD, suggesting a peak in global mean AOD values around June.

We further calculated the stratospheric ADRE using both the stratospheric kernels developed here and the kernels from YH23. The YH23 kernels, although based on total column aerosols, have been used in stratospheric ADRE quantifications in Schoeberl et al. (2023, 2024).

By including YH23 kernels in the comparison, we show the discrepancies that would be caused by kernels not specifically made for stratospheric aerosols. Figure 7b shows the stratospheric ADRE from the Hunga Eruption in 2022. For comparison, the RRTMG-calculated results based on the band-by-band AOD inputs are indicated by the red line. In general, the ADRE peaks with AOD near June, and using the band-by-band aerosol kernels can quantify it most accurately. The performance of broadband and physically sorted stratospheric aerosol kernels is slightly worse than that of the band-by-band kernels, as they fail to capture the wavelength dependency information and the Angstrom exponent assumption may be inadequate. In terms of global mean values, using the YH23 clear-sky kernel overestimates the cooling effect of the Hunga eruption, while using the YH23 all-sky kernel underestimates it.

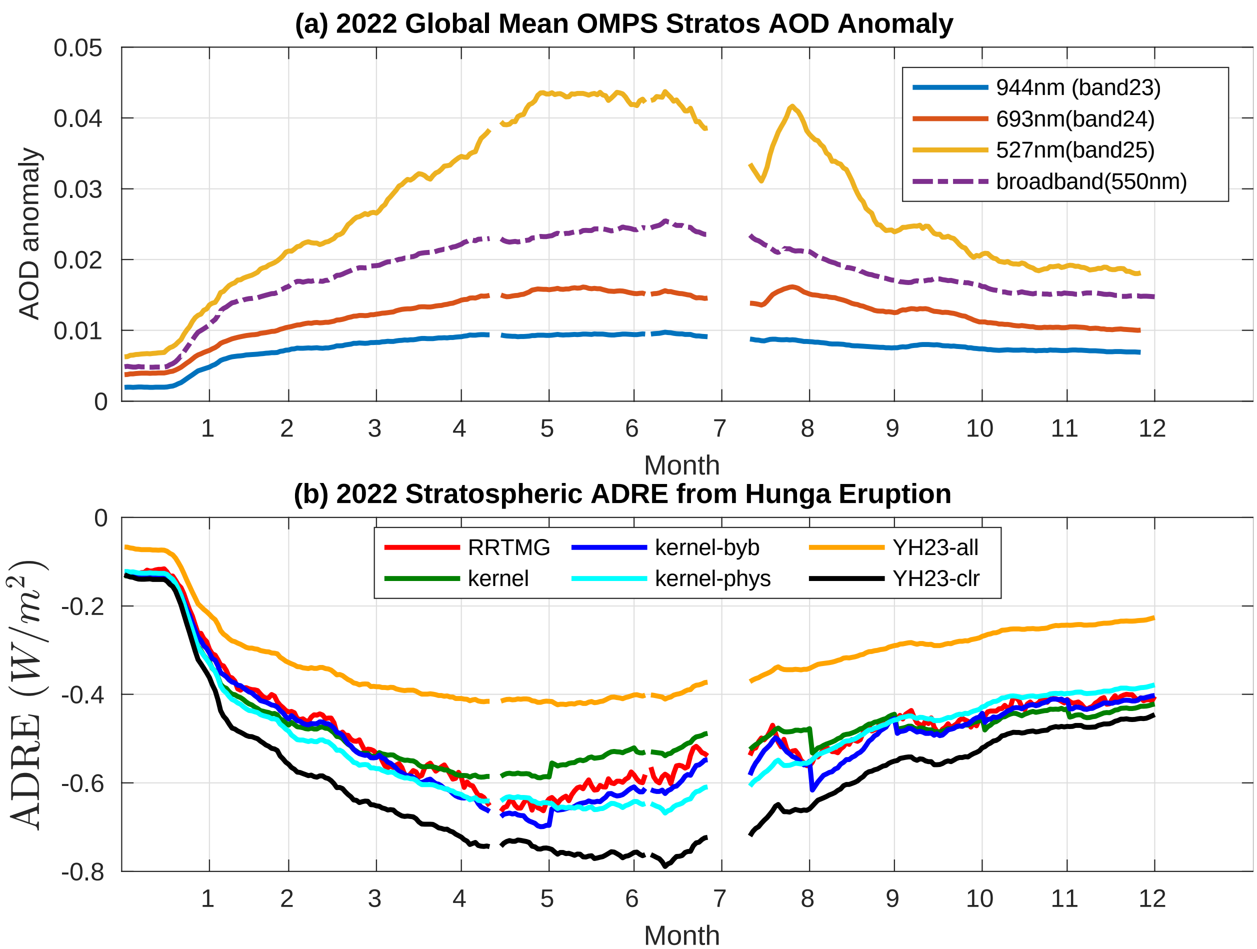

Figure 7. Time series of the global mean (a) stratospheric AOD anomaly from OMPS-LP following the Hunga Eruption in 2022 and (b) stratospheric ADRE from Hunga Eruption in 2022. YH23-clr and YH23-all represent the clear-sky and all-sky scattering AOD radiative sensitivity quantified in Q. Yu & Huang (2023b), respectively. Kernel, kernel-phys, and kernel-byb indicate the broadband kernels calculated from RRTMG, broadband kernels from the regression model, and the band-by-band kernels, respectively.

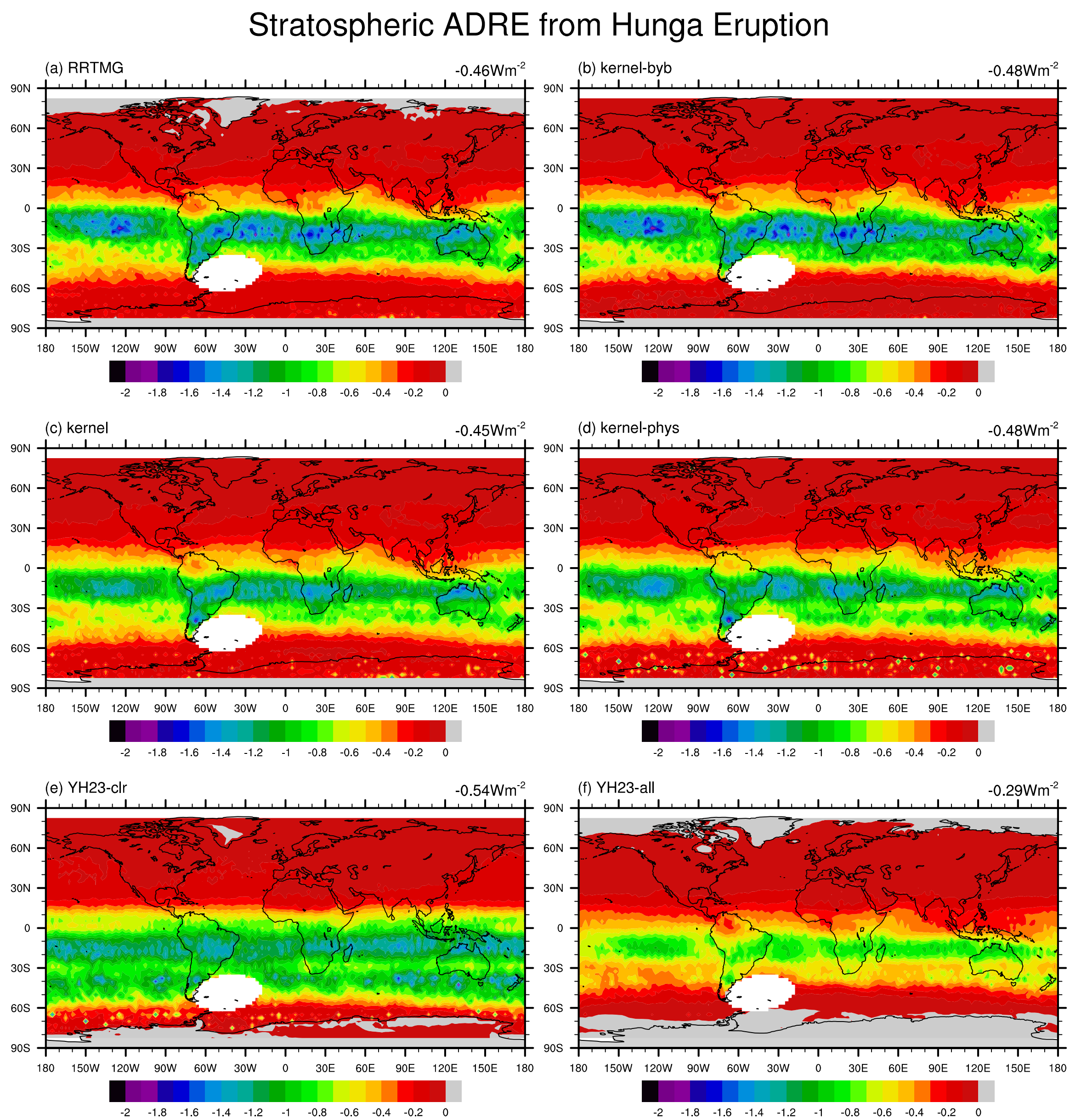

Figure 8. Annual mean stratospheric ADRE from the Hunga eruption in 2022, with global mean values indicated in the top right of each subplot. (a) RRTMG benchmark calculations; (b) Band-by-band kernel quantifications; (c) Broadband kernel quantifications; (d) Physically sorted kernel quantifications; (e) YH23 clear-sky kernel quantifications; (f) YH23 all-sky kernel quantifications. Global mean values are shown in the top right of each subplot.

Apart from the time evolution, we also compare the spatial patterns of stratospheric ADRE using different kernel schemes. Figure 8 displays the annual mean stratospheric ADRE from the Hunga eruption calculated from RRTMG as well as the kernels developed in this work. Results show that the volcanic eruption caused a uniform cooling in the southern hemisphere's tropical and subtropical regions due to the dispersion of aerosols described before. In terms of global mean ADRE, the Hunga eruption induced a cooling of -0.46 W/m^2. All stratospheric kernels developed in this work can reproduce the spatial features of ADRE relatively well, with the band-by-band kernels performing the best. Although the YH23 clear-sky scheme can approximately reproduce the global mean stratospheric ADRE values, it fails to capture the spatial patterns, especially over the cloudy regions.

Table 2 listed the R^2 and RMSE values comparing the ADRE induced by the Hunga eruption, calculated using different kernel schemes and the RRTMG model. Globally, the band-by-band, broadband, and physically sorted aerosol kernels capture 98.89%, 93.83%, and 94.33% of the variance in RRTMG-calculated ADRE, with RMSEs less than 0.04 W/m² (approximately 8.7% relative to the global mean values). Using YH23 kernels results in RMSEs greater than 0.11 W/m², which is 23.91% relative to the global mean.

Table 2. Performance of stratospheric kernels calculated in this study and kernels from YH23 in quantifying the ADRE of the 2022 Hunga volcanic eruption and 2020 Australia wildfire. R^2 represents the coefficient of determination, and RMSE is the Root Mean Squared Error. Relative errors are calculated by dividing the RMSE by the global mean values. Broadband and physically sorted kernels are used under the assumption of AE being 1.

	2022 Hunga volcanic eruption			2020 Australia wildfire		
	R^2	RMSE (W/m^2)	Relative errors	R^2	RMSE(W/m^2)	Relative errors
Band-by-band kernels	98.89%	0.02	4.35%	99.02%	0.01	3.57%
Broadband kernels	93.83%	0.04	8.70%	94.75%	0.04	14.29%
Physically sorted kernels	94.33%	0.04	8.70%	83.19%	0.08	28.57%
YH23-clr	95.11%	0.11	23.91%	83.59%	0.37	132.14%
YH23-all	91.88%	0.17	36.96%	51.32%	0.31	110.71%

4.3 2020 Australia Wildfire

In late December 2019, massive bushfires occurred in southeastern Australia and lifted a considerable amount of smoke into the stratosphere via pyrocumulonimbus clouds. Unlike the volcanic eruption case, we apply both the AOD_{scat} and AOD_{abs} kernels to study the stratospheric ADRE of the black-carbon-containing smoke particles as they are partly absorbing.

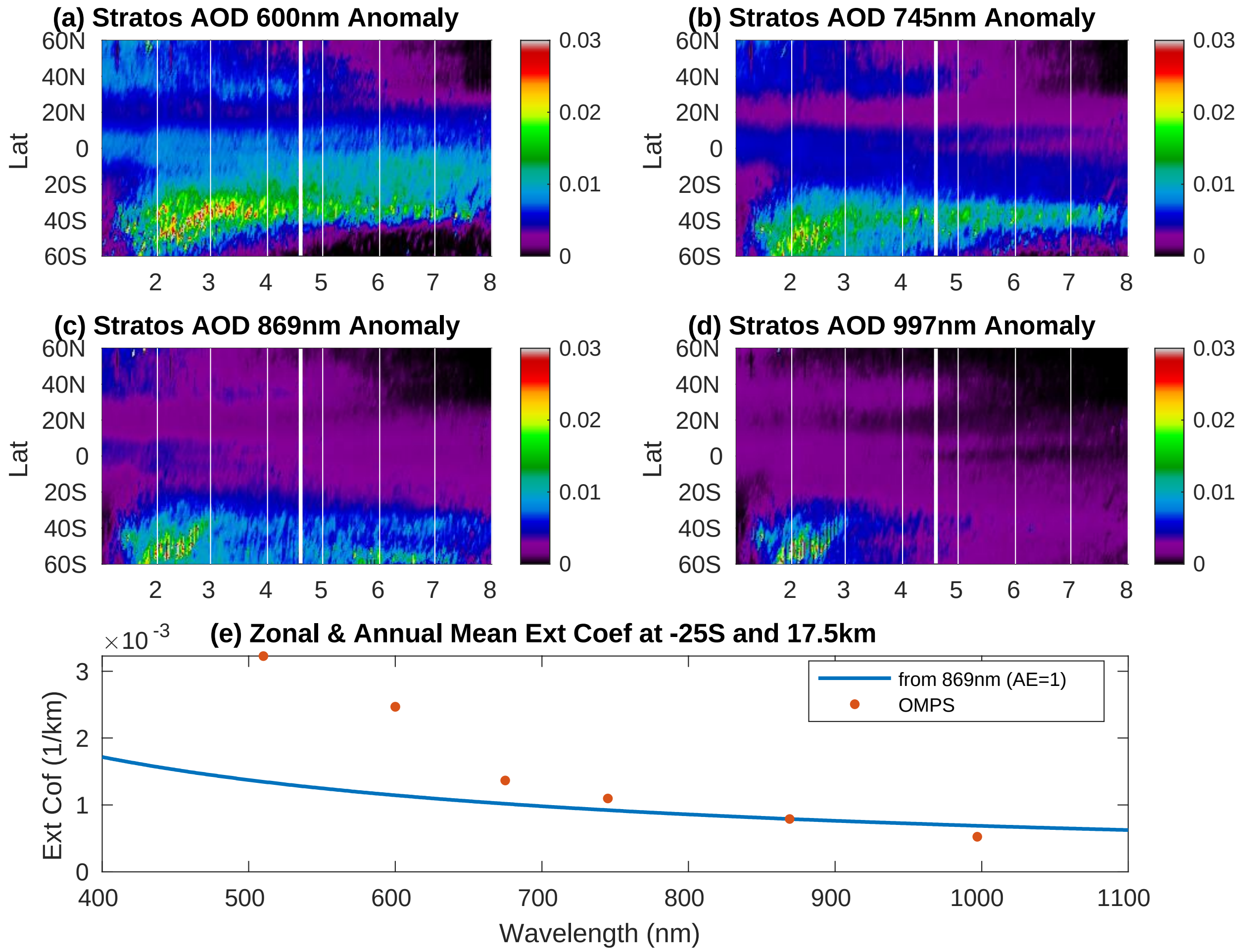

Figure 9. Same as Figure 6, but for the year 2020.

Figure 9 shows the zonal mean stratospheric AOD anomaly at different wavelengths, over 8 months starting in January 2020. After several periods of intense fires in early January 2020, the stratospheric AOD reached a maximum in early February and decayed afterward. The delay in reaching the AOD peaks might be due to the subsequent self-lofting of upper tropospheric aerosols, caused by buoyancy changes from the aerosols absorbing solar radiation (Ohneiser et al., 2020). After being lifted, aerosols spread equatorward and dilute significantly, leading to a decrease in the stratospheric AOD anomaly which lasts around eight months. Same as Figure 6e, Figure 9e also suggests that the AOD wavelength dependency relationship is complex, and assuming a certain Angstrom exponent may not be sufficient to represent the band-by-band AOD.

To investigate the performance of kernels in quantifying wildfire-related events, we assume the stratospheric aerosol anomaly consists of aged biomass burning aerosols with a single scattering albedo at 550 nm of 0.86 as suggested by recent studies (Damany-Pearce et al., 2022; Ohneiser et al., 2020). Figure 10a shows the global mean stratospheric AOD anomaly in the mid-visible bands in 2020. The interpolated AOD at RRTMG bands shows distinct differences compared to the broadband AOD, especially in February. Broadband AOD is calculated from scaling 869 nm to 550 nm assuming an AE of 1. Stratospheric ADRE is further calculated with known AOD and SSA. Figure 10b shows ADRE calculated from the RRTMG as well as kernel methods. Results show that using YH23 kernel schemes significantly underestimates the warming effect of stratospheric aerosols. This is because the stratospheric AOD_{abs} kernels are nearly twice as large as the YH-clearsky AOD_{abs} kernels, whereas the AOD_{scat} kernels show similar magnitudes compared with the YH-clearsky values (Figure 5b and Figure S9 in the Supporting Information). These results further emphasize the need to use kernels specifically designed for stratospheric aerosols to accurately quantify ADRE. As a comparison, using the stratospheric aerosol kernels captures wildfire-induced ADRE relatively well. The agreements in ADRE calculations indicate that our stratospheric aerosol kernel dataset is applicable for quantifying ADRE regardless of aerosol types (either scattering or absorbing). For the Australia wildfire, the carbonaceous aerosols led to a peak global mean warming of over +0.4 W/m^2 in mid-February 2020.

Figure 11 shows the comparison of the spatial distributions of ADRE calculated by different kernel schemes. Similar to the Hunga volcanic eruption case, the band-by-band kernel quantifications align most closely with the RRTMG-calculated results, with the R^2 being 99.02% (Table 2). Both the broadband and the physically sorted kernels slightly overestimate the aerosol warming, especially in the high-latitude regions. The slightly lower performance of broadband and physically sorted kernels in capturing the spatial patterns of ADRE might come from the bias in AOD_{550}, as using a uniform AE value for AOD wavelength conversion across the globe may not be representative. This aligns with other studies indicating that the Angstrom exponent can vary significantly (Malinina et al., 2019), particularly during wildfire events when the inclusion of organics can complicate the particle size distribution interpretation (Bourassa et al., 2019). Overall, the stratospheric kernels can capture more than 83.19% of the variance in the Australia wildfire-induced ADRE, with the RMSEs less than 0.08 W/m^2 (i.e. 28.57% relative to the global mean). Both Figure 11 and Table 2 suggest that YH23 kernel schemes are not suitable for quantifying the wildfire-dominated stratospheric ADRE because of its significant underestimation of AOD_{abs} kernels.

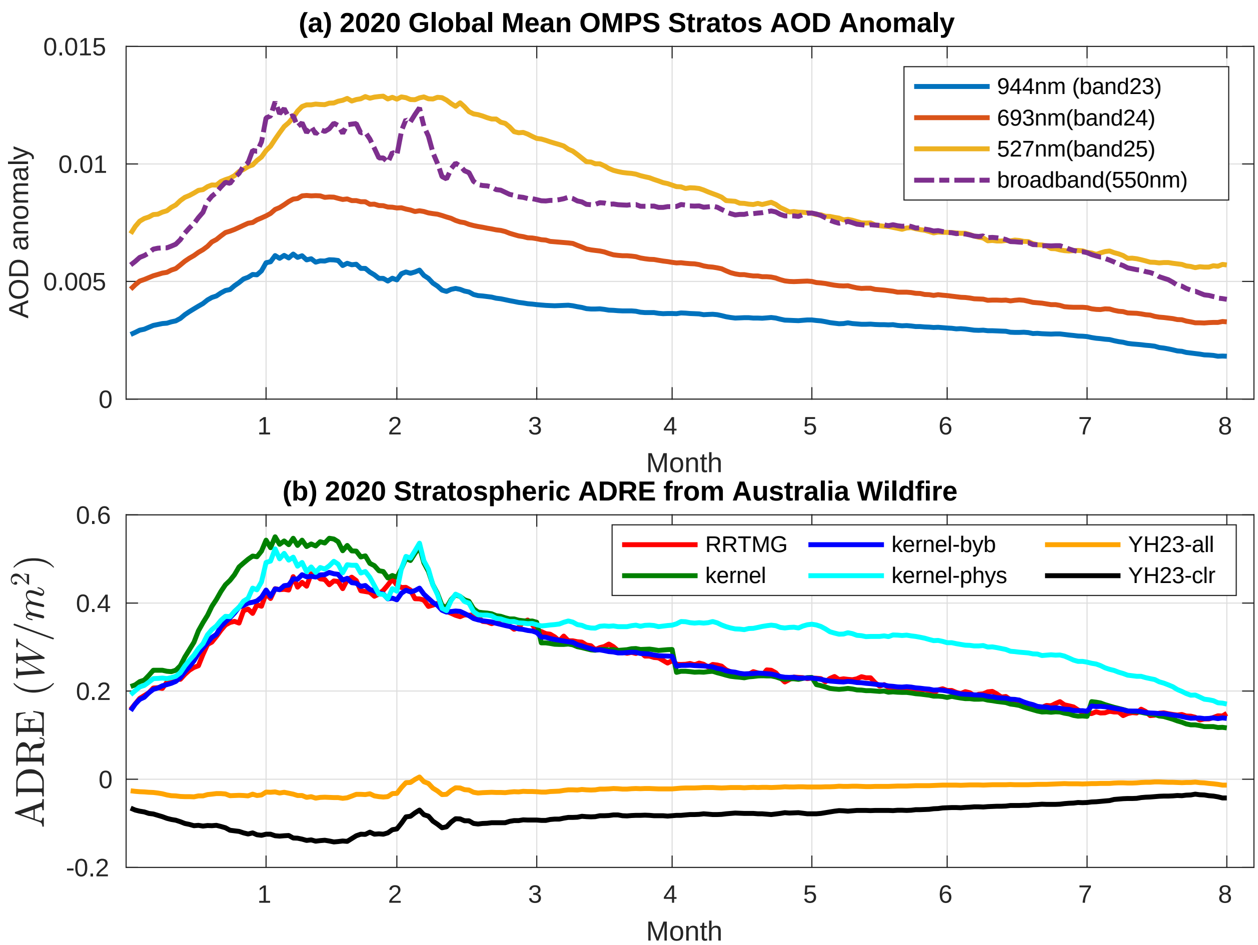

Figure 10. Same as Figure 7 but for the 2020 Australia wildfire.

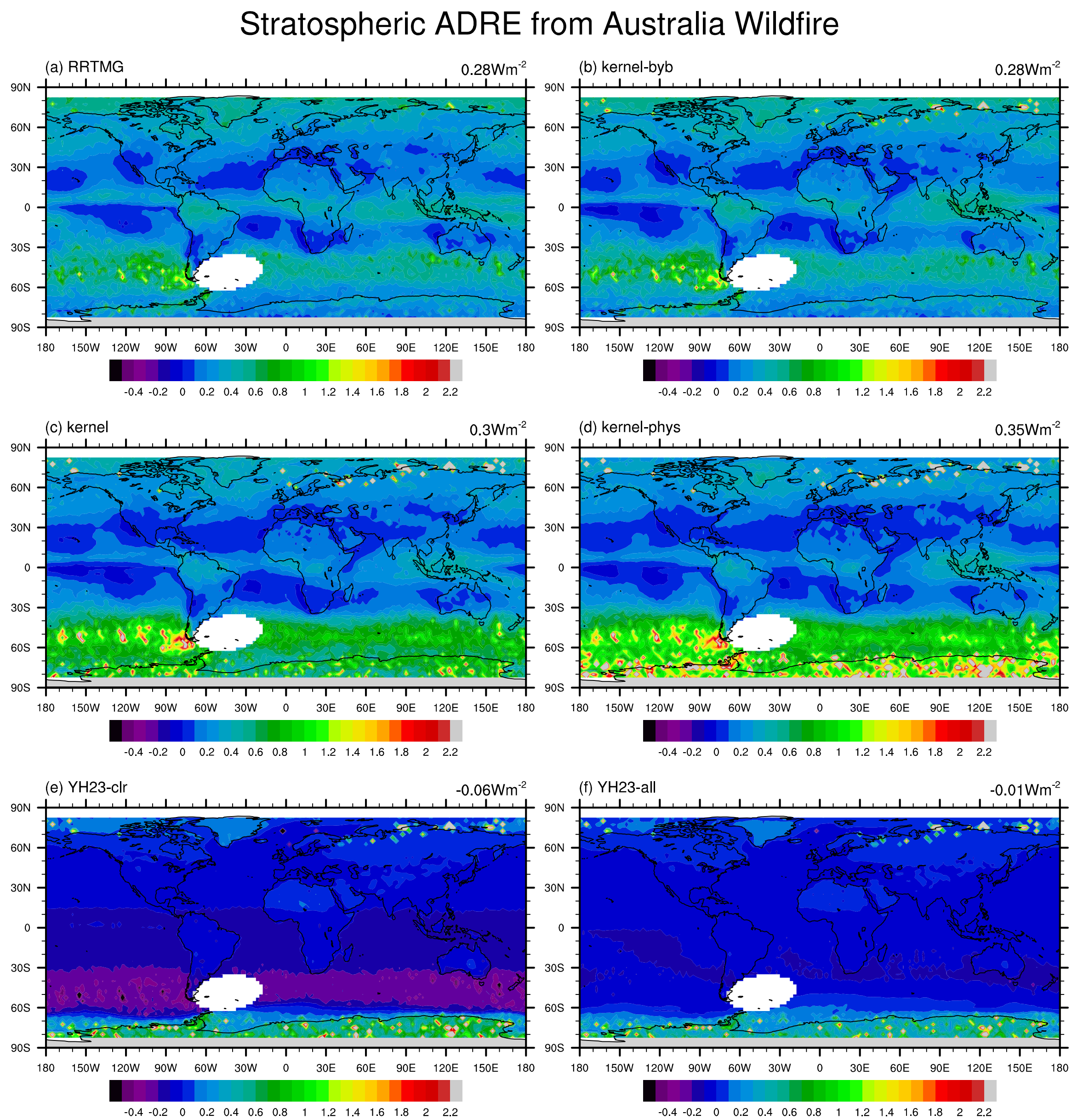

Figure 11. Same as Figure 8 but for the 2020 Australia wildfire.

5 Conclusions

This paper provides, for the first time, a comprehensive set of radiative kernels for stratospheric aerosols. The kernels are derived for the scattering and absorbing aerosol optical depth, respectively, based on partial radiative perturbation (PRP) computations using one year of 3-hourly MERRA-2 data. We analyzed the spatial variability of broadband aerosol kernels, demonstrating that they can be emulated as a joint function of solar insolation, TOA reflectance, and stratospheric aerosol optical depth. The developed aerosol radiative kernels provide a versatile tool for assessing the stratospheric ADRE of different aerosol types.

Stratospheric aerosol kernels exhibit significant spatial, temporal, and spectral variability (Figures 1-3). Validation tests have been done to evaluate the aerosol height dependency, linear scaling, and linear additivity of the kernels (Figures S4-S6). On a global scale, a 0.1 increase in stratospheric AOD_{scat}^{550} leads to a cooling effect of -2.65 W/m^2 at the TOA, while a similar increase in AOD_{abs}^{550} results in a warming effect of +41.95 W/m^2 (Figure 1). The magnitude of stratospheric aerosol kernels is greater than that for tropospheric aerosols (e.g., Thorsen et al., 2020; Q. Yu & Huang, 2023b), particularly for absorbing aerosols. This is due to the higher placement of aerosols, which interact with radiation less attenuated by clouds or tropospheric absorbers. Additionally, underlying clouds enhance the brightness of dark surfaces, thus amplifying the sensitivity of stratospheric ADRE to absorbing aerosols. Band-by-band aerosol kernels were calculated for the 14 bands in RRTMG SW, with spectral signatures indicating peak sensitivity from the near ultraviolet to the near-infrared (bands 23 to 25, 442 nm-1242 nm) (Figure 3). Using discrete AOD observations at these wavelengths allows for a more accurate constraint on ADRE.

From the single-layer aerosol analytical model, we identified that broadband aerosol kernels are related to TOA insolation, tropospheric reflectance, and stratospheric aerosol optical depth. We proposed a physically sorted set of aerosol kernels using a multivariate regression model, which can effectively reproduce the RRTMG-calculated broadband kernels (Figure 4 & S8). These physically sorted kernels are independent from geophysical location and can provide first-order estimations of stratospheric ADRE using satellite measurements.

The kernels were applied to calculate the ADRE for two stratospheric aerosol injection events: the 2022 Hunga volcanic eruption and the 2020 Australia wildfire. There is overall good agreement between the RRTMG-calculated results and those obtained using the kernels (Figures 7-8, Figures 10-11, Table 2). Band-by-band kernels perform best by constraining the wavelength dependency of AOD. Using band-by-band kernels can reproduce 99% of the ADRE variance with relative errors of less than 4%. Using other stratospheric kernels can capture more than 90% of the variance with relative errors of less than 10% (Table 2), despite the uncertainty in AE. The stratospheric ADRE from the 2022 Hunga eruption peaked six months after the event, inducing a global mean cooling of -0.46 W/m^2 (Figures 7-8). For the 2020 Australia wildfire, the stratospheric ADRE peaks one month after the event and results in a global mean warming of +0.28 W/m^2 from January to August (Figures 10-11).

To accurately calculate stratospheric ADRE, users are recommended to use the band-by-band kernels when reliable spectral AOD data is available. If such information is unavailable, the broadband aerosol kernels can be used alternatively, although the results should be used with caution as the broadband kernels are calculated based on an assumed Angstrom Exponent of 1. The physically sorted kernels have the advantage of not being restricted to specific geographical locations. With climate change, the aerosol-related and environmental conditions at a location may change. In such cases, physically sorted kernels may have an advantage for the ADRE quantification. Considering that there may be rapid stratospheric temperature adjustments in response to the instantaneous perturbations of the aerosols, the kernels developed in this work can be extended to include the radiative effects of such adjustments in future work, to provide an estimation of the effective (adjusted) radiative effect of the stratospheric aerosols.

Acknowledgments

We acknowledge the funding from the Natural Sciences and Engineering Research Council of Canada (RGPIN-2019-04511) and Canadian Space Agency (24SUHAWCSD) for supporting this research.

Data Availability Statement

The Modern-Era Retrospective Analysis for Research and Applications, Version 2 (MERRA-2) data used to calculate stratospheric aerosol kernels are provided by NASA Global Modeling and Assimilation Office (Randles et al., 2017). The aerosol mixing ratio, assimilated meteorological fields, radiation and aerosol diagnostics data are available at Global Modeling and Assimilation Office via https://doi.org/10.5067/LTVB4GPCOTK2, https://doi.org/10.5067/WWQSXQ8IVFW8, https://doi.org/10.5067/Q9QMY5PBNV1T and https://doi.org/10.5067/KLICLTZ8EM9D (Gelaro et al., 2017). The dataset of stratospheric aerosol direct radiative effect kernels (monthly mean broadband, band-by-band, and the annual mean physically sorted ones), along with the scripts and data to reproduce the findings in this paper, are available on Mendeley Data at https://data.mendeley.com/datasets/t87tfnk2xd/1

References

Ångström, A. (1929). On the atmospheric transmission of sun radiation and on dust in the air. *Geografiska Annaler*, *11*(2), 156–166.

Ayash, T., Gong, S. L., Jia, C. Q., Huang, P., Zhao, T. L., & Lavoue, D. (2008). Global modeling of multicomponent aerosol species: Aerosol optical parameters. *Journal of Geophysical Research: Atmospheres*, *113*(D12). https://doi.org/10.1029/2007JD008968

Balmes, K. A., & Fu, Q. (2021). All-Sky Aerosol Direct Radiative Effects at the ARM SGP Site. *Journal of Geophysical Research: Atmospheres*, *126*(17), e2021JD034933. https://doi.org/10.1029/2021JD034933

Bourassa, A. E., Rieger, L. A., Zawada, D. J., Khaykin, S., Thomason, L. W., & Degenstein, D. A. (2019). Satellite Limb Observations of Unprecedented Forest Fire Aerosol in the Stratosphere. *Journal of Geophysical Research: Atmospheres*, *124*(16), 9510–9519. https://doi.org/10.1029/2019JD030607

Bourassa, A. E., Zawada, D. J., Rieger, L. A., Warnock, T. W., Toohey, M., & Degenstein, D. A. (2023). Tomographic Retrievals of Hunga Tonga-Hunga Ha'apai Volcanic Aerosol. *Geophysical Research Letters*, *50*(3), e2022GL101978. https://doi.org/10.1029/2022GL101978

Chauvigné, A., Waquet, F., Auriol, F., Blarel, L., Delegove, C., Dubovik, O., Flamant, C., Gaetani, M., Goloub, P., Loisil, R., Mallet, M., Nicolas, J.-M., Parol, F., Peers, F., Torres, B., & Formenti, P. (2021). Aerosol above-cloud direct radiative effect and properties in the Namibian region during the AErosol, RadiatiOn, and CLOuds in southern Africa (AEROCLO-sA) field campaign – Multi-Viewing, Multi-Channel, Multi-Polarization (3MI) airborne simulator and sun photometer measurements. *Atmospheric Chemistry and Physics*, *21*(10), 8233–8253. https://doi.org/10.5194/acp-21-8233-2021

Chen, Z., Bhartia, P. K., Torres, O., Jaross, G., Loughman, R., DeLand, M., Colarco, P., Damadeo, R., & Taha, G. (2020). Evaluation of the OMPS/LP stratospheric aerosol extinction product using SAGE III/ISS observations. *Atmospheric Measurement Techniques*, *13*(6), 3471–3485. https://doi.org/10.5194/amt-13-3471-2020

Chlek, P., & Coakley Jr, J. A. (1974). Aerosols and climate. *Science*, *183*(4120), 75–77.

Damany-Pearce, L., Johnson, B., Wells, A., Osborne, M., Allan, J., Belcher, C., Jones, A., & Haywood, J. (2022). Australian wildfires cause the largest stratospheric warming since Pinatubo and extends the lifetime of the Antarctic ozone hole. *Scientific Reports*, *12*(1), 12665. https://doi.org/10.1038/s41598-022-15794-3

Datseris, G., Blanco, J., Hadas, O., Bony, S., Caballero, R., Kaspi, Y., & Stevens, B. (2022). Minimal Recipes for Global Cloudiness. *Geophysical Research Letters*, *49*(20), e2022GL099678. https://doi.org/10.1029/2022GL099678

Flynn, L. E., Seftor, C. J., Larsen, J. C., & Xu, P. (2006). The ozone mapping and profiler suite. In *Earth Science Satellite Remote Sensing: Vol. 1: Science and Instruments* (pp. 279–296). Springer.

Fromm, M., Lindsey, D. T., Servranckx, R., Yue, G., Trickl, T., Sica, R., Doucet, P., & Godin-Beekmann, S. (2010). The untold story of pyrocumulonimbus. *Bulletin of the American Meteorological Society*, *91*(9), 1193–1210.

Gao, J., Huang, Y., Peng, Y., & Wright, J. S. (2023). Aerosol Effects on Clear-Sky Shortwave Heating in the Asian Monsoon Tropopause Layer. *Journal of Geophysical Research: Atmospheres*, *128*(4), e2022JD036956. https://doi.org/10.1029/2022JD036956

Gelaro, R., McCarty, W., Suárez, M. J., Todling, R., Molod, A., Takacs, L., Randles, C. A., Darmenov, A., Bosilovich, M. G., Reichle, R., Wargan, K., Coy, L., Cullather, R., Draper, C., Akella, S., Buchard, V., Conaty, A., Silva, A. M. da, Gu, W., … Zhao, B. (2017). The Modern-Era Retrospective Analysis for Research and Applications, Version 2 (MERRA-2). *Journal of Climate*, *30*(14), 5419–5454. https://doi.org/10.1175/JCLI-D-16-0758.1 [dataset]

Giles, D. M., Sinyuk, A., Sorokin, M. G., Schafer, J. S., Smirnov, A., Slutsker, I., Eck, T. F., Holben, B. N., Lewis, J. R., Campbell, J. R., Welton, E. J., Korkin, S. V., & Lyapustin, A. I. (2019). Advancements in the Aerosol Robotic Network (AERONET) Version 3 database – automated near-real-time quality control algorithm with improved cloud screening for Sun photometer aerosol optical depth (AOD) measurements. *Atmospheric Measurement Techniques*, *12*(1), 169–209. https://doi.org/10.5194/amt-12-169-2019

Grinsted, A., Moore, J. C., & Jevrejeva, S. (2007). Observational evidence for volcanic impact on sea level and the global water cycle. *Proceedings of the National Academy of Sciences*, *104*(50), 19730–19734. https://doi.org/10.1073/pnas.0705825104

Günther, M., Schmidt, H., Timmreck, C., & Toohey, M. (2024). Why does stratospheric aerosol forcing strongly cool the warm pool? *Atmospheric Chemistry and Physics*, *24*(12), 7203–7225. https://doi.org/10.5194/acp-24-7203-2024

Hansen, J. (2005). Efficacy of climate forcings. *Journal of Geophysical Research*, *110*(D18), D18104. https://doi.org/10.1029/2005JD005776

Haywood, J. M., & Shine, K. P. (1995). The effect of anthropogenic sulfate and soot aerosol on the clear sky planetary radiation budget. *Geophysical Research Letters*, *22*(5), 603–606. https://doi.org/10.1029/95GL00075

Heald, C. L., Ridley, D. A., Kroll, J. H., Barrett, S. R. H., Cady-Pereira, K. E., Alvarado, M. J., & Holmes, C. D. (2014). Contrasting the direct radiative effect and direct radiative forcing of aerosols. *Atmospheric Chemistry and Physics*, *14*(11), 5513–5527. https://doi.org/10.5194/acp-14-5513-2014

Huang, Y., Tan, X., & Xia, Y. (2016). Inhomogeneous radiative forcing of homogeneous greenhouse gases: Inhomogeneous Forcing of Homogeneous Gas. *Journal of Geophysical Research: Atmospheres*, *121*(6), 2780–2789. https://doi.org/10.1002/2015JD024569

Kloss, C., Sellitto, P., Renard, J.-B., Baron, A., Bègue, N., Legras, B., Berthet, G., Briaud, E., Carboni, E., Duchamp, C., Duflot, V., Jacquet, P., Marquestaut, N., Metzger, J.-M., Payen, G., Ranaivombola, M., Roberts, T., Siddans, R., & Jégou, F. (2022). Aerosol Characterization of the Stratospheric Plume From the Volcanic Eruption at Hunga Tonga

15 January 2022. *Geophysical Research Letters*, *49*(16), e2022GL099394. https://doi.org/10.1029/2022GL099394

Kremser, S., Thomason, L. W., von Hobe, M., Hermann, M., Deshler, T., Timmreck, C., Toohey, M., Stenke, A., Schwarz, J. P., Weigel, R., Fueglistaler, S., Prata, F. J., Vernier, J.-P., Schlager, H., Barnes, J. E., Antuña-Marrero, J.-C., Fairlie, D., Palm, M., Mahieu, E., … Meland, B. (2016). Stratospheric aerosol—Observations, processes, and impact on climate. *Reviews of Geophysics*, *54*(2), 278–335. https://doi.org/10.1002/2015RG000511

Liu, C.-C., Portmann, R. W., Liu, S., Rosenlof, K. H., Peng, Y., & Yu, P. (2022). Significant Effective Radiative Forcing of Stratospheric Wildfire Smoke. *Geophysical Research Letters*, *49*(17), e2022GL100175. https://doi.org/10.1029/2022GL100175

Loeb, N. G., Wang, H., Rose, F. G., Kato, S., Smith, W. L., & Sun-Mack, S. (2019). Decomposing Shortwave Top-of-Atmosphere and Surface Radiative Flux Variations in Terms of Surface and Atmospheric Contributions. *Journal of Climate*, *32*(16), 5003–5019. https://doi.org/10.1175/JCLI-D-18-0826.1

MacMartin, D. G., Kravitz, B., Tilmes, S., Richter, J. H., Mills, M. J., Lamarque, J.-F., Tribbia, J. J., & Vitt, F. (2017). The Climate Response to Stratospheric Aerosol Geoengineering Can Be Tailored Using Multiple Injection Locations. *Journal of Geophysical Research: Atmospheres*, *122*(23), 12,574-12,590. https://doi.org/10.1002/2017JD026868

Malinina, E., Rozanov, A., Rieger, L., Bourassa, A., Bovensmann, H., Burrows, J. P., & Degenstein, D. (2019). Stratospheric aerosol characteristics from space-borne observations: Extinction coefficient and Ångström exponent. *Atmospheric Measurement Techniques*, *12*(7), 3485–3502. https://doi.org/10.5194/amt-12-3485-2019

Martinsson, B. G., Friberg, J., Sandvik, O. S., Hermann, M., van Velthoven, P. F. J., & Zahn, A. (2019). Formation and composition of the UTLS aerosol. *Npj Climate and Atmospheric Science*, *2*(1), 1–6. https://doi.org/10.1038/s41612-019-0097-1

McComiskey, A., Schwartz, S. E., Schmid, B., Guan, H., Lewis, E. R., Ricchiazzi, P., & Ogren, J. A. (2008). Direct aerosol forcing: Calculation from observables and sensitivities to inputs. *Journal of Geophysical Research*, *113*(D9), D09202. https://doi.org/10.1029/2007JD009170

Mlawer, E. J., Iacono, M. J., Pincus, R., Barker, H. W., Oreopoulos, L., & Mitchell, D. L. (2016). Contributions of the ARM Program to Radiative Transfer Modeling for Climate and Weather Applications. *Meteorological Monographs*, *57*(1), 15.1-15.19. https://doi.org/10.1175/AMSMONOGRAPHS-D-15-0041.1

Mlawer, E. J., Taubman, S. J., Brown, P. D., Iacono, M. J., & Clough, S. A. (1997). Radiative transfer for inhomogeneous atmospheres: RRTM, a validated correlated-k model for the longwave. *Journal of Geophysical Research: Atmospheres*, *102*(D14), 16663–16682. https://doi.org/10.1029/97JD00237

Ohneiser, K., Ansmann, A., Baars, H., Seifert, P., Barja, B., Jimenez, C., Radenz, M., Teisseire, A., Floutsi, A., Haarig, M., Foth, A., Chudnovsky, A., Engelmann, R., Zamorano, F., Bühl, J., & Wandinger, U. (2020). Smoke of extreme Australian bushfires observed in the stratosphere over Punta Arenas, Chile, in January 2020: Optical thickness, lidar ratios, and depolarization ratios at 355 and 532 nm. *Atmospheric Chemistry and Physics*, *20*(13), 8003–8015. https://doi.org/10.5194/acp-20-8003-2020

Ohneiser, K., Ansmann, A., Witthuhn, J., Deneke, H., Chudnovsky, A., Walter, G., & Senf, F. (2023). Self-lofting of wildfire smoke in the troposphere and stratosphere: Simulations and space lidar observations. *Atmospheric Chemistry and Physics*, *23*(4), 2901–2925. https://doi.org/10.5194/acp-23-2901-2023

Randles, C. A., A. M. da Silva, V. Buchard, A. Darmenov, P. R. Colarco, V. Aquila, H. Bian, E. P. Nowottnick, X. Pan, A. Smirnov, H. Yu, and R. Govindaraju, 2016. The MERRA-2 Aerosol Assimilation. *NASA Technical Report Series on Global Modeling and Data Assimilation, NASA/TM-2016-104606*, Vol. **45**, 143 pp. [Available online at https://gmao.gsfc.nasa.gov/pubs/docs/Randles887.pdf]

Randles, C. A., Silva, A. M. da, Buchard, V., Colarco, P. R., Darmenov, A., Govindaraju, R., Smirnov, A., Holben, B., Ferrare, R., Hair, J., Shinozuka, Y., & Flynn, C. J. (2017). The MERRA-2 Aerosol Reanalysis, 1980 Onward. Part I: System Description and Data Assimilation Evaluation. *Journal of Climate*, *30*(17), 6823–6850. https://doi.org/10.1175/JCLI-D-16-0609.1 [dataset]

Reddy, M. S., Boucher, O., Balkanski, Y., & Schulz, M. (2005). Aerosol optical depths and direct radiative perturbations by species and source type. *Geophysical Research Letters*, *32*(12). https://doi.org/10.1029/2004GL021743

Robock, A. (2000). Volcanic eruptions and climate. *Reviews of Geophysics*, *38*(2), 191–219.

Schoeberl, M. R., Wang, Y., Taha, G., Zawada, D. J., Ueyama, R., & Dessler, A. (2024a). Evolution of the Climate Forcing During the Two Years After the Hunga Tonga-Hunga Ha'apai Eruption. *Journal of Geophysical Research: Atmospheres*, *129*(14), e2024JD041296. https://doi.org/10.1029/2024JD041296

Schoeberl, M. R., Wang, Y., Taha, G., Zawada, D. J., Ueyama, R., & Dessler, A. E. (2024b). *Evolution of the Climate Forcing During the Two Years after the Hunga Tonga-Hunga Ha'apai Eruption*. https://doi.org/10.22541/essoar.171288896.63010190/v1

Schoeberl, M. R., Wang, Y., Ueyama, R., Dessler, A., Taha, G., & Yu, W. (2023). The Estimated Climate Impact of the Hunga Tonga-Hunga Ha'apai Eruption Plume. *Geophysical Research Letters, 50*(18), e2023GL104634. https://doi.org/10.1029/2023GL104634

Schuster, G. L., Dubovik, O., & Holben, B. N. (2006). Angstrom exponent and bimodal aerosol size distributions. *Journal of Geophysical Research: Atmospheres, 111*(D7). https://doi.org/10.1029/2005JD006328

Sellitto, P., Belhadji, R., Kloss, C., & Legras, B. (2022). Radiative impacts of the Australian bushfires 2019–2020 – Part 1: Large-scale radiative forcing. *Atmospheric Chemistry and Physics, 22*(14), 9299–9311. https://doi.org/10.5194/acp-22-9299-2022

Sellitto, P., Belhadji, R., Legras, B., Podglajen, A., & Duchamp, C. (2024). *The optical properties of stratospheric aerosol layer perturbation of the Hunga volcano eruption of January 15th, 2022*. https://doi.org/10.5194/egusphere-2024-1433

Strahan, S. E., Oman, L. D., Douglass, A. R., & Coy, L. (2015). Modulation of Antarctic vortex composition by the quasi-biennial oscillation. *Geophysical Research Letters*, *42*(10), 4216–4223. https://doi.org/10.1002/2015GL063759

Taha, G., Loughman, R., Colarco, P. R., Zhu, T., Thomason, L. W., & Jaross, G. (2022). Tracking the 2022 Hunga Tonga-Hunga Ha'apai Aerosol Cloud in the Upper and Middle Stratosphere Using Space-Based Observations. *Geophysical Research Letters*, *49*(19), e2022GL100091. https://doi.org/10.1029/2022GL100091

Taha, G., Loughman, R., Zhu, T., Thomason, L., Kar, J., Rieger, L., & Bourassa, A. (2021). OMPS LP Version 2.0 multi-wavelength aerosol extinction coefficient retrieval algorithm.

Atmospheric Measurement Techniques, *14*(2), 1015–1036. https://doi.org/10.5194/amt-14-1015-2021

Thorsen, T. J., Ferrare, R. A., Kato, S., & Winker, D. M. (2020). Aerosol Direct Radiative Effect Sensitivity Analysis. *Journal of Climate*, *33*(14), 6119–6139. https://doi.org/10.1175/JCLI-D-19-0669.1

Visioni, D., MacMartin, D. G., Kravitz, B., Lee, W., Simpson, I. R., & Richter, J. H. (2020). Reduced Poleward Transport Due to Stratospheric Heating Under Stratospheric Aerosols Geoengineering. *Geophysical Research Letters*, *47*(17), e2020GL089470. https://doi.org/10.1029/2020GL089470

Wang, X., Randel, W., Zhu, Y., Tilmes, S., Starr, J., Yu, W., Garcia, R., Toon, O. B., Park, M., Kinnison, D., Zhang, J., Bourassa, A., Rieger, L., Warnock, T., & Li, J. (2023). Stratospheric Climate Anomalies and Ozone Loss Caused by the Hunga Tonga-Hunga Ha'apai Volcanic Eruption. *Journal of Geophysical Research: Atmospheres*, *128*(22), e2023JD039480. https://doi.org/10.1029/2023JD039480

Weisenstein, D. K., Keith, D. W., & Dykema, J. A. (2015). Solar geoengineering using solid aerosol in the stratosphere. *Atmospheric Chemistry and Physics*, *15*(20), 11835–11859. https://doi.org/10.5194/acp-15-11835-2015

Wu, C.-H., Lee, S.-Y., Tsai, I.-C., Shiu, C.-J., & Chen, Y.-Y. (2023). Volcanic contribution to the 1990s North Pacific climate shift in winter. *Scientific Reports*, *13*(1), 5672. https://doi.org/10.1038/s41598-023-32956-z

Yu, P., Portmann, R. W., Peng, Y., Liu, C.-C., Zhu, Y., Asher, E., Bai, Z., Lu, Y., Bian, J., Mills, M., Schmidt, A., Rosenlof, K. H., & Toon, O. B. (2023). Radiative Forcing From the

2014–2022 Volcanic and Wildfire Injections. *Geophysical Research Letters*, *50*(13), e2023GL103791. https://doi.org/10.1029/2023GL103791

Yu, Qiurun (2024), "Quantifying the Direct Radiative Effect of Stratospheric Aerosols Using Radiative Kernels", Mendeley Data, V1, doi: 10.17632/t87tfnk2xd.1 [dataset]

Yu, Q., & Huang, Y. (2023a). A Dissection of the Inter-Model Spread of the Aerosol Direct Radiative Effect in CMIP6 Models. *Geophysical Research Letters*, *50*(21), e2023GL105112. https://doi.org/10.1029/2023GL105112

Yu, Q., & Huang, Y. (2023b). Distributions and Trends of the Aerosol Direct Radiative Effect in the 21st Century: Aerosol and Environmental Contributions. *Journal of Geophysical Research: Atmospheres*, *128*(4). https://doi.org/10.1029/2022JD037716

Yu, Q., Jervis, D., & Huang, Y. (2024). Accounting for the effect of aerosols in GHGSat methane retrieval. *Atmospheric Measurement Techniques*, *17*(11), 3347–3366. https://doi.org/10.5194/amt-17-3347-2024

Yu, Q.-R., Zhang, F., Li, J., & Zhang, J. (2019). Analysis of sea-salt aerosol size distributions in radiative transfer. *Journal of Aerosol Science*, *129*, 71–86. https://doi.org/10.1016/j.jaerosci.2018.11.014

Journal of Geophysical Research: Atmosphere

Supporting Information for

Quantifying the Direct Radiative Effect of Stratospheric Aerosols Using Radiative Kernels

Qiurun Yu[1], Yi Huang[1]

[1] Department of Atmospheric and Oceanic Sciences, McGill University, Montreal, Quebec, Canada.

Contents of this file

Figures S1 to S9
Tables S1 to S2

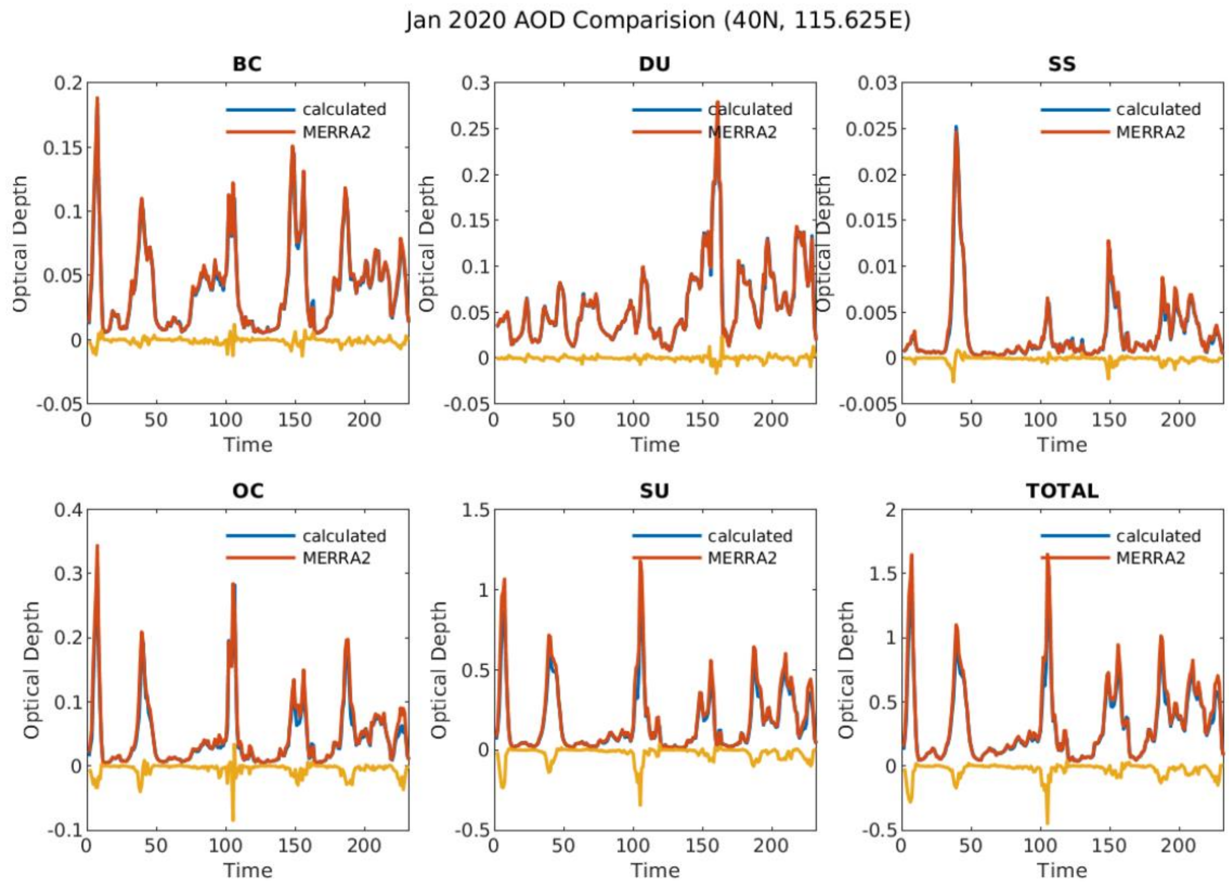

Figure S1. Validation of total column aerosol optical depth (AOD) reconstructed from MERRA-2 aerosol mixing ratio data for black carbon (BC), dust (DU), sea salt (SS), organic carbon (OC), and sulfate (SU) aerosols. The validation is conducted for Beijing, China, in January 2020.

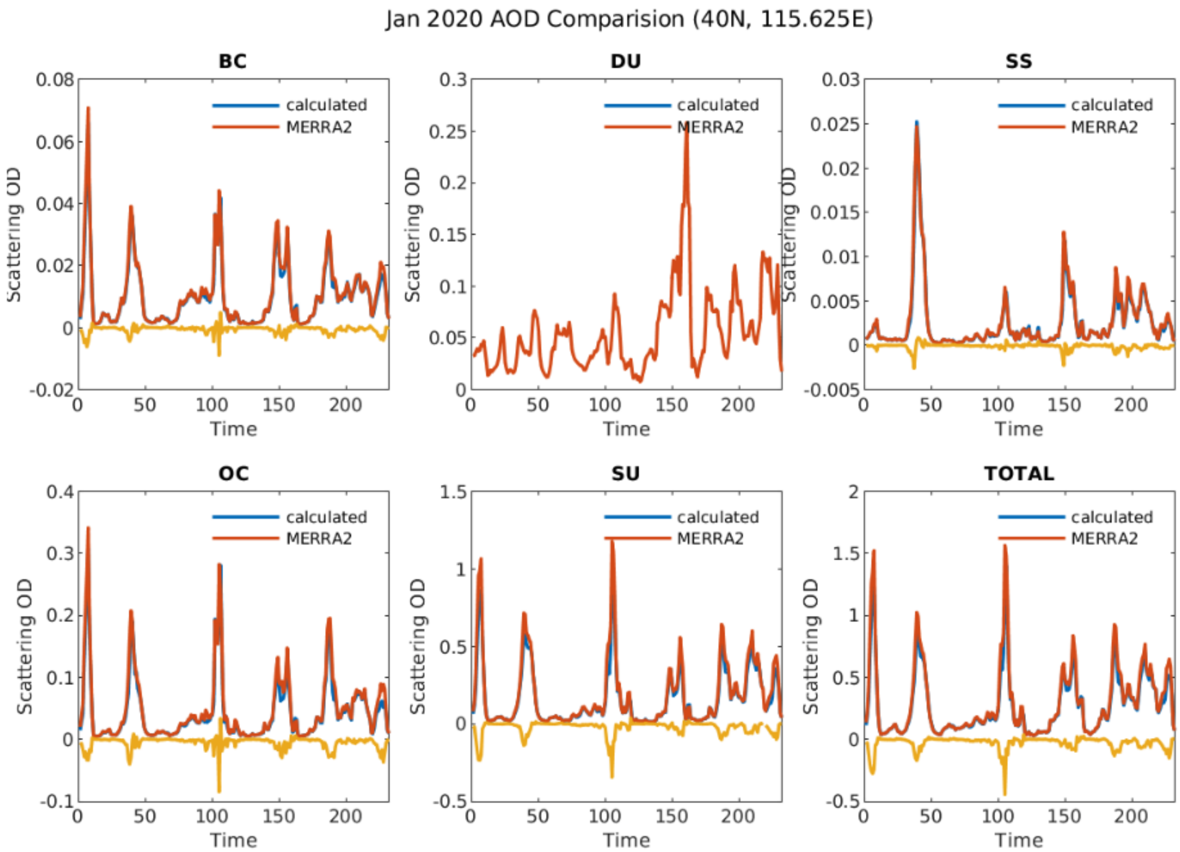

Figure S2. The same as Figure S1 but for total column scattering aerosol optical depth.

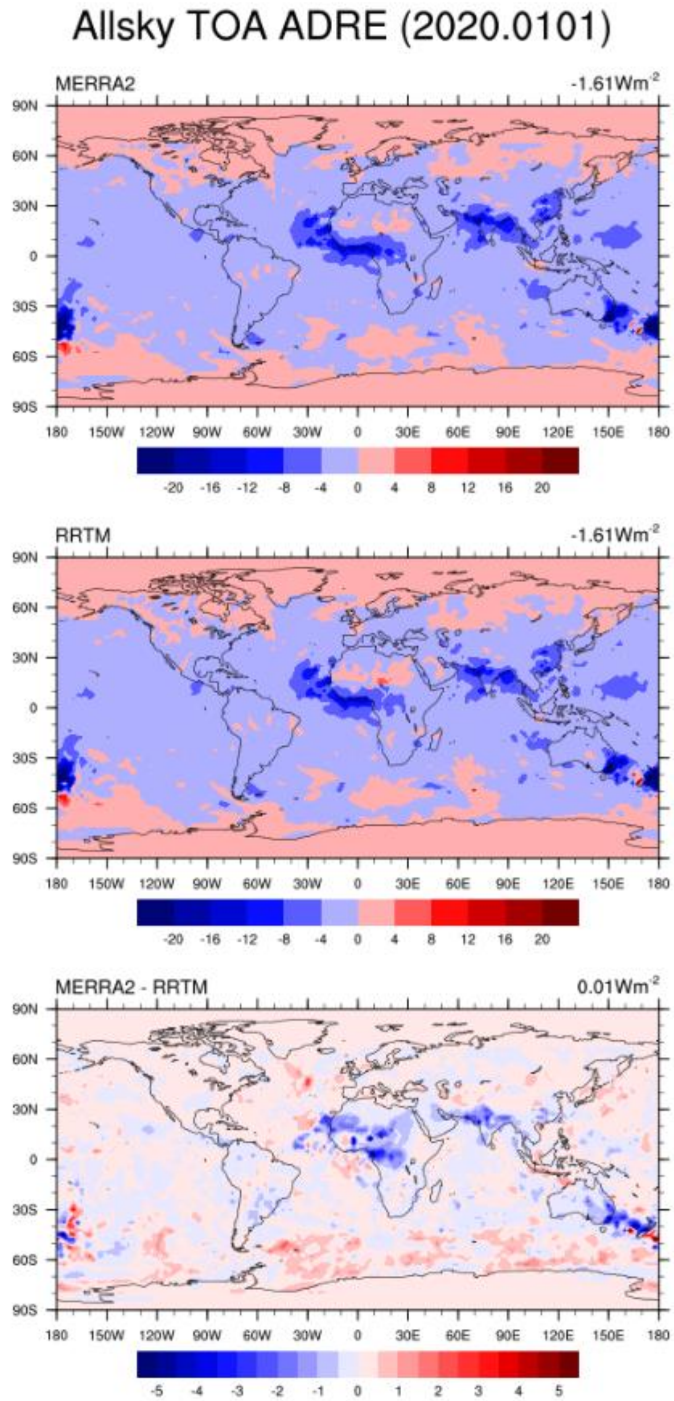

Figure S3. Validation of all-sky total column ADRE calculations using RRMTG for January 1st, 2020. Upper: ADRE from MERRA2; Middle: RRTMG-calculated ADRE; Bottom: Bias.

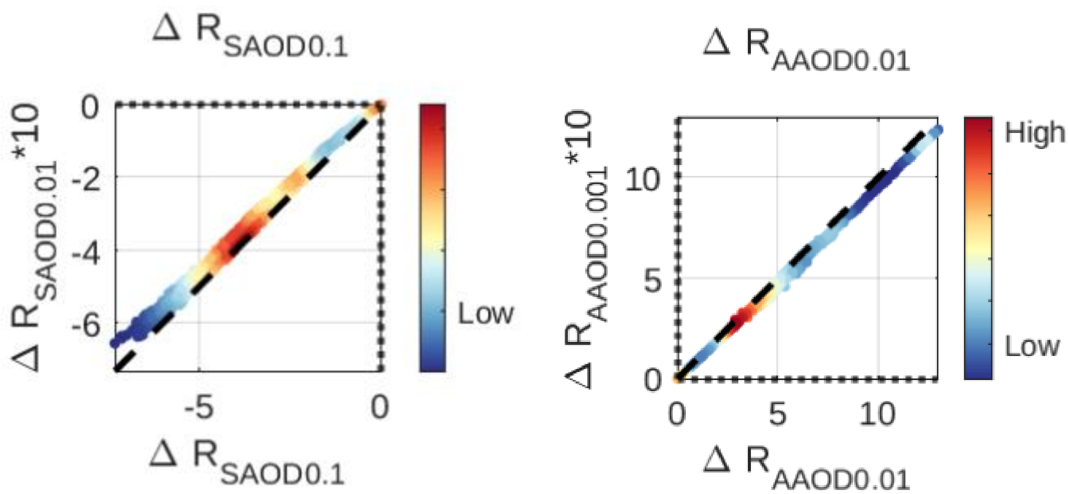

Figure S4. Linear scaling test for broadband Top-Of-Atmosphere (TOA) flux changes (ΔR) in response to perturbations in stratospheric scattering and absorbing AOD. Aerosols are placed at the 1st layer above tropopause. The scattering AOD perturbations are 0.1 and 0.01, while the absorbing AOD perturbations are 0.01 and 0.001, respectively.

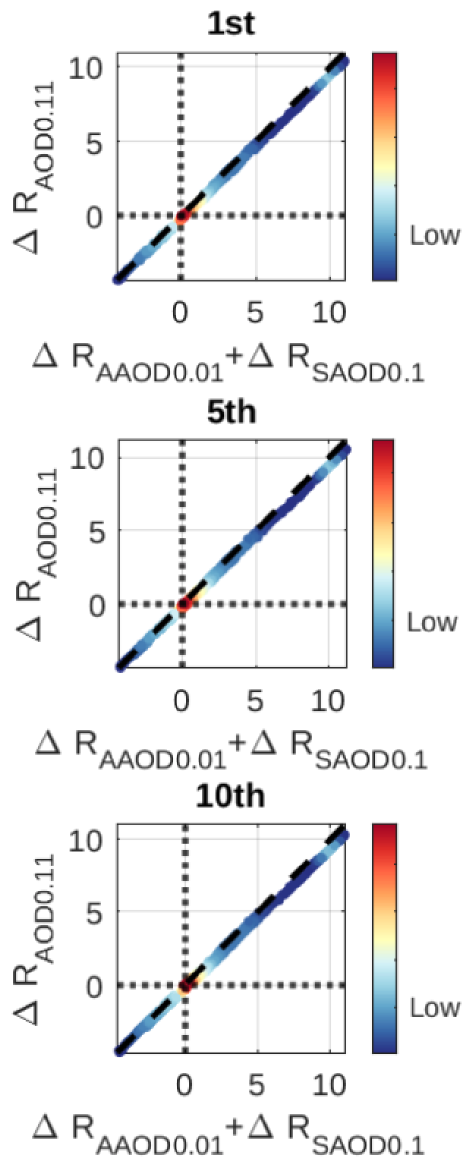

Figure S5. linear additivity test for broadband TOA flux changes (ΔR) in response to perturbations in both stratospheric scattering and absorbing AOD. Aerosols are positioned at the 1st, 5th, and 10th layer above the tropopause, respectivly. The perturbations are set to 0.1 for scattering AOD and 0.01 for absorbing AOD. The summed ΔR for scattering and absorbing AOD perturbations shows good agreement with the results from total AOD perturbations.

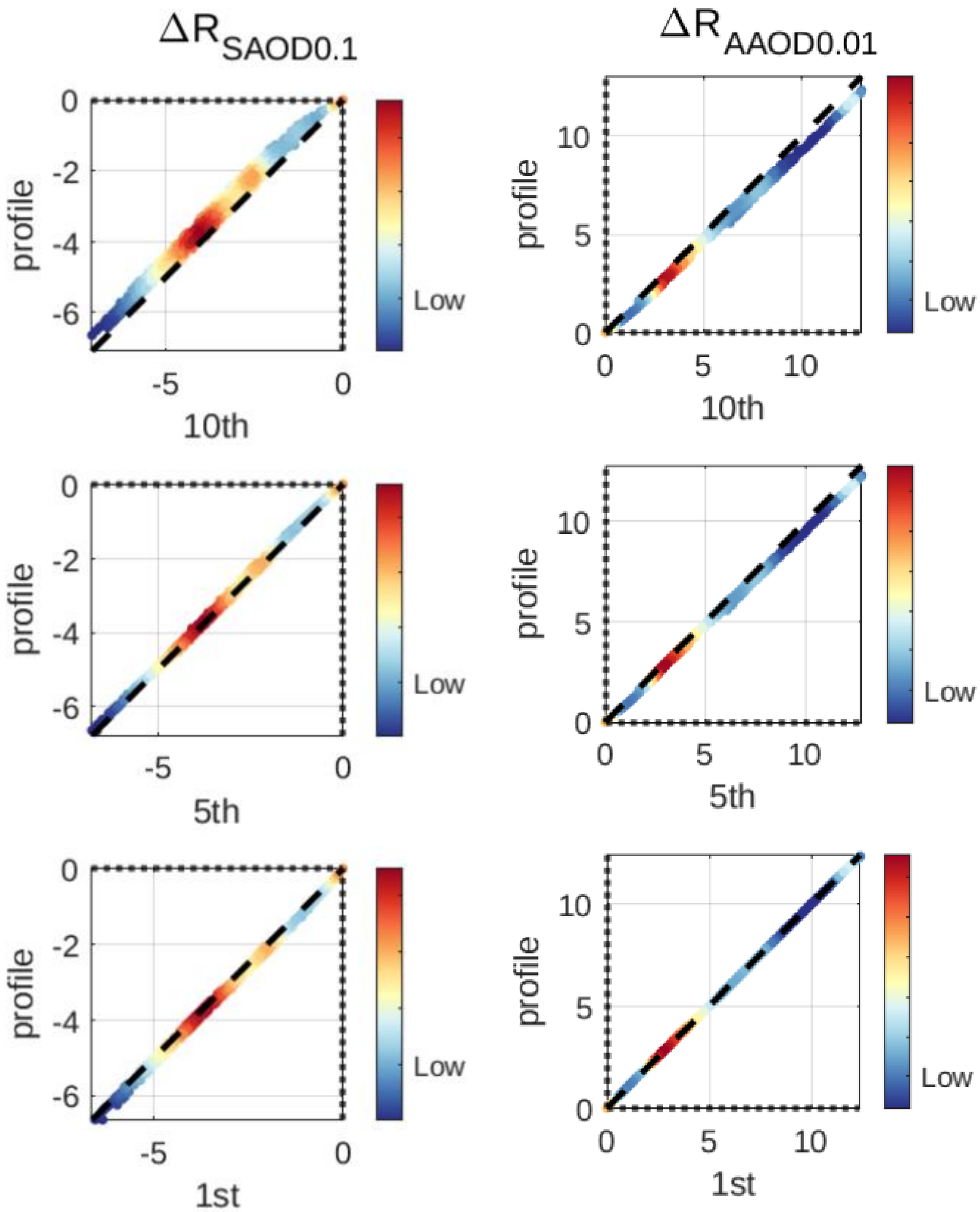

Figure S6. height dependency test for broadband TOA flux changes (ΔR) in response to aerosol perturbation layer height. The ADRE results from perturbing AOD at a single radom layer (e.g., 1st, 5th, 10th above the tropopause) are similar to those obtained from perturbing the entire stratospheric aerosol profiles.

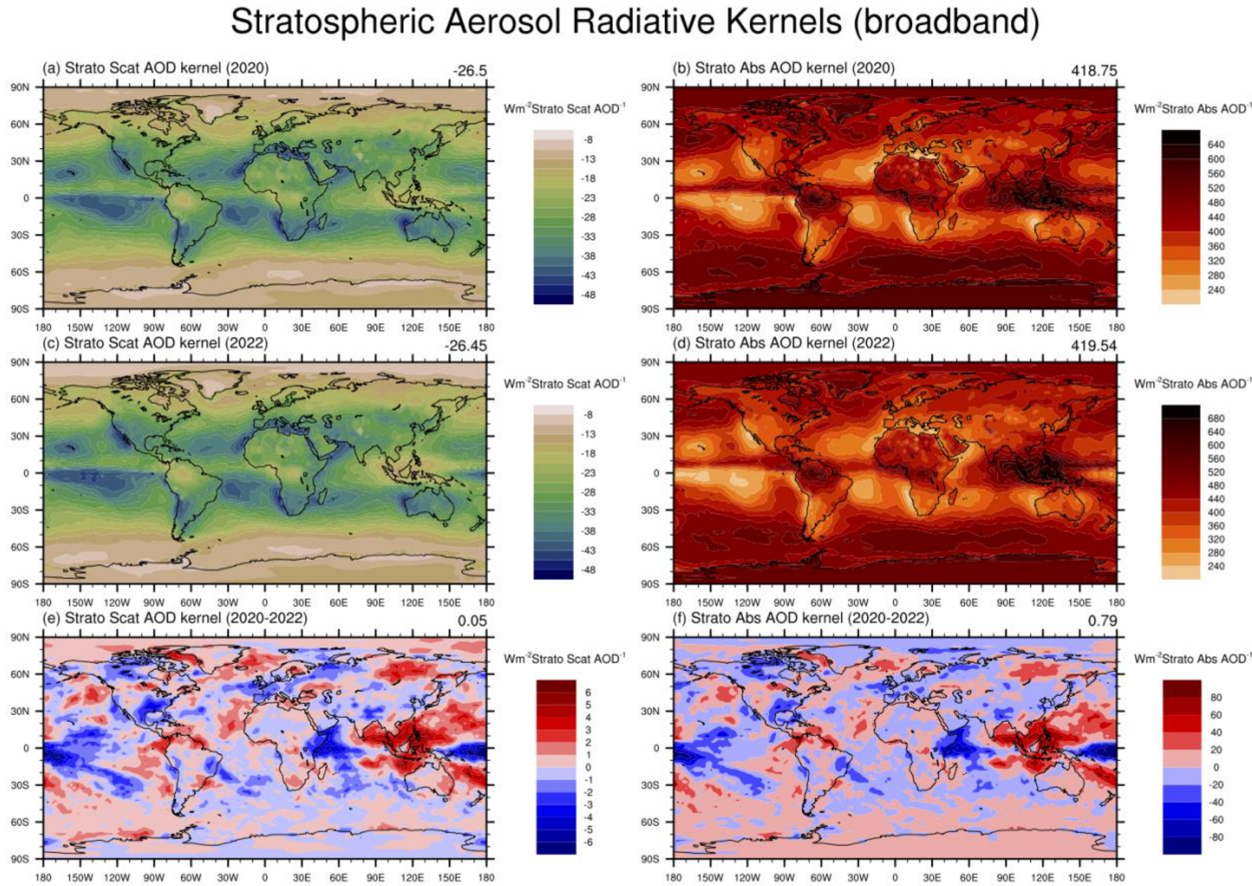

Figure S7. Comparisons between the annual mean stratospheric AOD_{scat} and AOD_{abs} kernels for the years 2020 and 2022. First row: 2020; Middle row: 2022; Bottom row: differences (2020-2022).

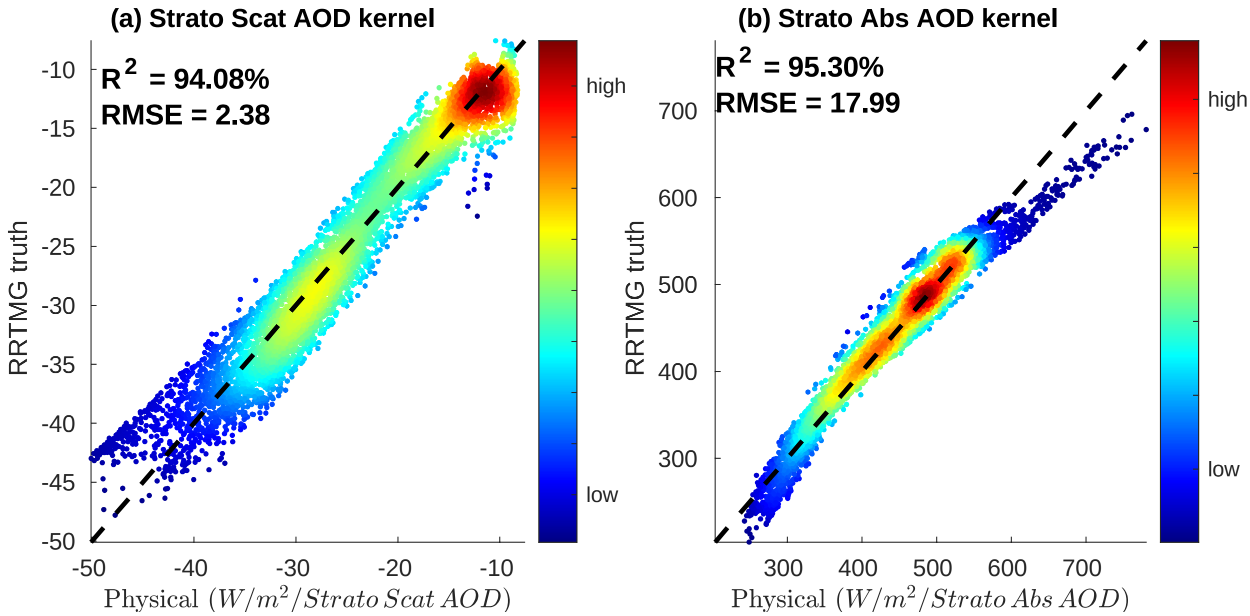

Figure S8. Validations of the physically sorted broadband aerosol kernels for stratospheric AOD_{scat} and AOD_{abs} against benchmark RRTMG calculations.

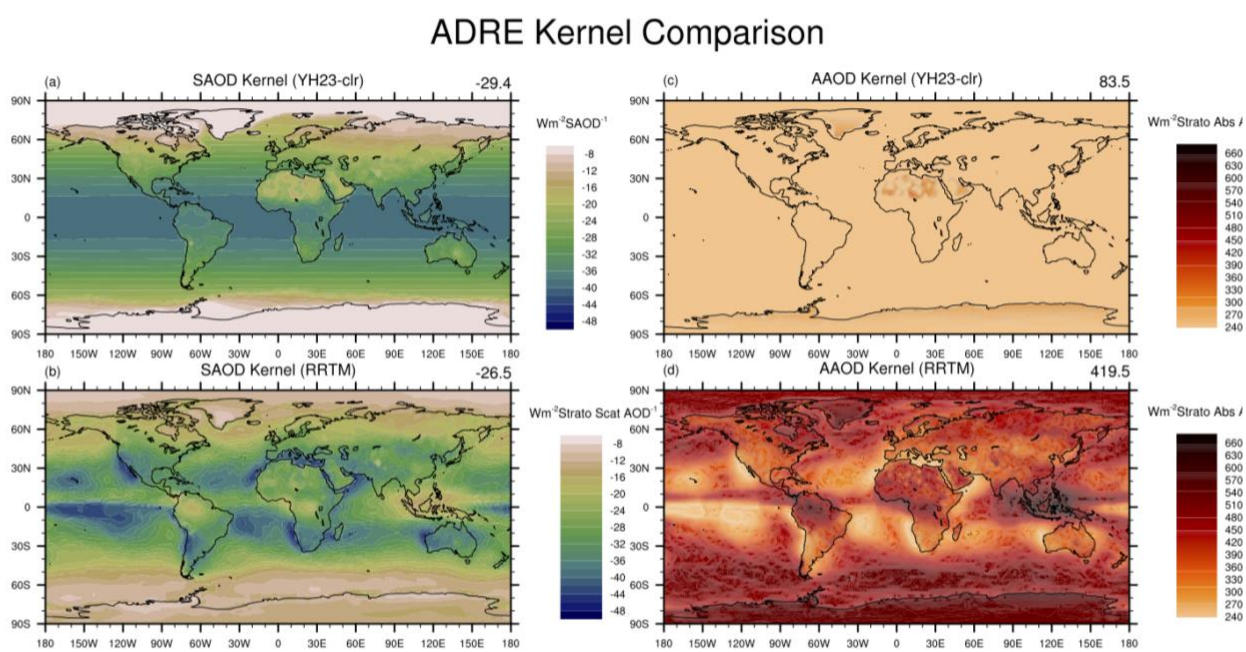

Figure S9. Comparisons between the stratospheric ADRE kernels developed in this work and the YH23 clear-sky kernels for total column aerosols. Left column: kernels for AOD_{scat}; Right column: kernels for AOD_{abs}

Table 1 Evaluation of predictor performance for SAOD kernels normalized by insolation ($\frac{1}{S}\frac{\partial ADRE}{\partial SAOD}$). R is the TOA reflectance and τ is the stratospheric aerosol optical depth. R^2 represents the coefficient of determination, and RMSE is the Root Mean Squared Error.

1 predictor	R_s	R_s^2	τ	R_s τ	-	-
R^2	86.04%	84.21%	69.82%	73.18%	-	-
RMSE	3.40	3.63	4.75	4.51	-	-
2 predictors	(R_s τ& (R_s^2)	(R_s τ& (τ	(R_sτ& (R_s)	(R_s^2) & (τ	(R_s) & (τ	(R_s^2) & (R_s)
R^2	92.50%	83.87%	92.50%	91.72%	93.91%	87.30%
RMSE	2.27	3.55	2.27	2.44	2.02	3.15
3 predictors	(R_s^2) & (R_s) & (τ)	(R_s^2) & (R_s) & (R_s τ)	(R_s^2) & (τ) & (R_s τ)			
R^2	94.01%	93.55%	92.50%	-	-	-
RMSE	rmse=2.99	rmse=3.06	rmse=3.26	-	-	-
4 predictors	(τ) & R_s^2 & (R_s) & (R_s τ)	-	-	-	-	-
R^2	94.08%	-	-	-	-	-
RMSE	2.38	-	-	-	-	-

Table 2 Evaluations of predictor performances for AAOD kernels normalized by insolation ($\frac{1}{S}\frac{\partial ADRE}{\partial AAOD}$). R is the TOA reflectance and τ is the stratospheric aerosol optical depth.

1 predictor	R_s	R_s^2	τ	R_s τ	-	-
R^2	74.03%	87.49%	1.97%	50.86%	-	-
RMSE	45.45	29.54	83.21	52.46	-	-
2 predictors	(R_s τ) & (R_s^2)	(R_s τ) & (τ)	(R_sτ) & (R_s)	(R_s^2) & (τ)	(R_s) & (τ)	(R_s^2) & (R_s)
R^2	90.43%	86.32%	82.59%	88.64%	76.37%	89.89%
RMSE	23.96	27.55	32.37	26.59	39.53	25.57
3 predictors	(R_s^2) & (R_s) & (τ)	(R_s^2) & (R_s) & (R_s τ)	(R_s^2) & (τ) & (R_s τ)			
R^2	90.43%	86.32%	82.59%	-	-	-
RMSE	23.96	27.55	32.37	-	-	-
4 predictors	(τ) & R_s^2 & (R_s) & (R_s τ)	-	-	-	-	-
R^2	95.30%	-	-	-	-	-
RMSE	17.99	-	-	-	-	-